

Model study of the cross-frontal water exchange on Georges Bank: A three-dimensional Lagrangian experiment

Changsheng Chen and Qichun Xu

School for Marine Science and Technology, University of Massachusetts-Dartmouth, New Bedford, Massachusetts, USA

Robert C. Beardsley

Department of Physical Oceanography, Woods Hole Oceanographic Institution, Woods Hole, Massachusetts, USA

Peter J. S. Franks

Marine Life Research Group, Scripps Institution of Oceanography, University of California, San Diego, La Jolla, California, USA

Received 21 April 2000; revised 26 June 2002; accepted 6 November 2002; published 13 May 2003.

[1] Characteristics of the cross-frontal water exchange over Georges Bank are investigated through a sequence of numerical model experiments featuring realistic three-dimensional (3-D) bathymetry, bi-monthly averaged climatological stratification, tidal forcing, and mean and observed wind-forcing. The model used in this study is the ECOM-si version of the *Blumberg and Mellor* [1987] primitive equation model with *Mellor-Yamada* [1982] level 2.5 turbulence closure. The model domain includes Georges Bank and the Gulf of Maine, and is forced at the open ocean boundary by the semidiurnal M_2 tide. Fluid particles were tracked in the 3-D, time-dependent Eulerian flow field to examine the Lagrangian flow field, and passive tracer experiments were conducted to investigate the relative roles of advection and turbulent diffusion on cross-frontal exchange. Two distinct paths for the on-bank water movement were detected on Georges Bank: one is over the northwestern flank of the bank where the bottom topography changes sharply in both along- and cross-bank directions, and the other is near the bottom around the bank where the tidal mixing front is located. Over the northern flank, the cross-bank component of the Lagrangian residual current is generally opposite in direction to that of the Eulerian residual current, resulting in an on-bank, cross-frontal water transport near the bottom. Over the southern flank, the near-bottom water tends to converge toward the tidal mixing and shelf-break fronts, so that the near-bottom flow over the shelf between these two fronts is divergent. The response to wind-forcing varied with ambient stratification and water depth. In winter, strong winds can drive a significant off-bank water transport, tending to “wash out” the bank. In summer, winds are generally too weak to alter the general pattern of tidal-driven particle motion within the mixed region on the crest of the bank and the surrounding tidal mixing front. Some wind-driven off-bank transport occurs near the surface in the stratified region on the outer southern flank, but this has little influence on water movement near the bottom. Passive tracer experiments reveal that the net cross-frontal water flux near the bottom is caused primarily by advection and horizontal diffusion. Tidal-induced vertical diffusion tends to make the tracer mix rapidly upward, thus reducing the percent of the cross-frontal flux due to advection. Our new model results are consistent with previous model studies of Georges Bank, and agree in general with drifter and dye patches observed in the U.S. GLOBEC NW Atlantic/Georges Bank program. *INDEX TERMS*: 4255 Oceanography: General: Numerical modeling; 4528 Oceanography: Physical: Fronts and jets; 4512 Oceanography: Physical: Currents; 4560 Oceanography: Physical: Surface waves and tides (1255); *KEYWORDS*: Georges Bank, cross-frontal exchange, Eulerian and Lagrangian residual currents, tidal mixing front, Stokes’ drift

Citation: Chen, C., Q. Xu, R. C. Beardsley, and P. J. S. Franks, Model study of the cross-frontal water exchange on Georges Bank: A three-dimensional Lagrangian experiment, *J. Geophys. Res.*, 108(C5), 3142, doi:10.1029/2000JC000390, 2003.

1. Introduction

[2] The cross-frontal exchange of water, nutrients and biota plays a critical role in the maintenance and evolution of the Georges Bank (GB) ecosystem. Strong semidiurnal tidal currents cause strong vertical mixing which results in a well-defined density front around the shallow crest of the Bank during spring throughfall [Flagg, 1987; Loder and Wright, 1985]. This front is located near the ~ 40 -m isobath on the northern flank and ~ 40 to 60-m isobaths over the eastern and southern flanks, which separates the mixed water on the top from the stratified water on the flank. The highest phytoplankton concentrations (as evidenced by chlorophyll-a) are generally found in the mixed area of the Bank though out spring and summer, indicating a significant flux of nutrients onto the Bank and across the tidal mixing front in addition to local recycling [Horne *et al.*, 1989; Franks and Chen, 1996]. Such fluxes are required to fuel the primary and secondary production on GB.

[3] Physical mechanisms responsible for cross-frontal transport have received considerable attention in the U.S. GLOBAL ECOSYSTEM (GLOBEC) NW Atlantic/Georges Bank program. Chen and Beardsley [1998] investigated the tidally-driven cross-bank residual flow using a two-dimensional (2-D) primitive equation model with cross-bank topography. They found that on-bank, cross-frontal transport could occur in the bottom boundary layer as a result of asymmetric tidal mixing over time. Further analysis by Pringle and Franks [2001] using an analytic bottom boundary layer model clearly illustrates this mechanism. Chen and Beardsley [1998] also found that the Lagrangian and Eulerian residual flows were generally in opposite directions over the steep northern slope during strong stratification conditions, providing a pathway for upslope nutrient supply during summer. The near-bottom, on-bank Lagrangian residual flow was described first by Loder *et al.* [1997]. Based on fluid particle tracking in a tidally-driven 3-D homogenous flow field, they found that the Stokes' drift contribution was similar in magnitude to the Eulerian residual flow, leading to on-bank water movement near the bottom.

[4] Despite these initial studies, the physical mechanisms that control the on-bank and cross-frontal transport of water and material on stratified GB are still not well examined. For example, are the results from the idealized 2-D model experiments of Chen and Beardsley [1998] and Franks and Chen [1996] still valid for realistic 3-D GB bathymetry? How does the Stokes' drift velocity and Lagrangian residual flow vary with stratification, bottom slope, and tidal intensity? How does water move in the bottom boundary layer on the southern flank between tidal mixing and shelf-break fronts? Where are the primary paths for on-bank and cross-frontal water movement on GB? These related questions about cross-frontal exchange on GB remain unanswered.

[5] This paper seeks to reexamine the influences of bottom topography, stratification, and wind-forcing on the Lagrangian residual circulation and cross-frontal exchange on GB. Roworth and Signell [1998] recently compiled a new high-resolution (15 sec in latitude and longitude spacing; ~ 0.5 km) U.S.G.S. digital bathymetric database for the Gulf of Maine (GOM)/GB domain. We used this database to configure a new 3-D primitive equation model, which Chen *et al.* [2001] used to investigate tidal simulation and the

formation of the tidal mixing fronts on the Bank. Here we use the model to conduct initial value experiments using both bi-monthly averaged climatological temperature and salinity fields and idealized stratification as initial conditions, open boundary tidal forcing, and mean and time-dependent surface wind stress forcing. Fluid particles were tracked in the resulting 3-D Eulerian flow fields to determine the Lagrangian flow over the Bank with special focus on on-bank and cross-frontal exchange. A semianalytical model was also developed to demonstrate the robustness of the Lagrangian residual flow fields predicted using the 3-D discrete numerical circulation model.

[6] The rest of this paper is structured as follows. The 3-D model and experimental design are described in section 2. The model results of the bi-monthly-averaged Eulerian, Lagrangian, and Stokes' drift currents are presented in sections 3 and 4. Characteristics of the 3-D particle motion over the Bank are examined in section 5, a passive tracer experiment is summarized in section 6, and analysis with a simple analytical model is presented in section 7. Discussion and conclusions are summarized in section 8.

2. The Model and Numerical Design

[7] The numerical model used in this study is the ECOM-si version of the 3-D coastal ocean circulation model developed originally by Blumberg and Mellor [1987]. The model incorporates the Mellor and Yamada [1974, 1982] level 2.5 turbulent closure scheme (MY2.5) as modified by Galperin *et al.* [1988] to provide a time and space-dependent parameterization of vertical turbulent mixing. The model uses the σ -coordinate in the vertical and curvilinear orthogonal coordinates in the horizontal. The model incorporates the semiimplicit scheme developed by Casulli [1990] that allows the barotropic pressure gradient in the momentum equations and the velocity convergence in the continuity equation to be treated implicitly. A detailed description of the model and GOM/GB configuration is given in Chen *et al.* [2001].

[8] The numerical model domain covers the GOM/GB region and is enclosed by an open boundary running from the New Jersey shelf to the Nova Scotia shelf (Figure 1). The orthogonal curvilinear coordinate system was chosen to give better horizontal resolution over the GOM/GB, varying from 1.5–3 km over GB and in the interior region of the GOM expanding to 4–20 km near the open boundary. Thirty-one uniform σ -levels were used in the vertical, providing 1.3–4 m vertical resolution over the depth range 40–120 m on GB, and 10 m over the off-bank depth of 300 m. The bottom depth at each model grid point was interpolated directly from the new USGS bathymetric database. The model time step was 207 sec, resulting in 216 time steps over a M_2 (12.42 hours) tidal cycle.

[9] The model is forced along the open boundary by the surface M_2 tidal elevation and phase taken from the global $0.5^\circ \times 0.5^\circ$ inverse tidal model of Egbert *et al.* [1994]. No flux boundary conditions for temperature and salinity are specified. A gravity wave radiation condition on current was applied at the open boundary to minimize energy reflection into the computational domain. To examine the impact of wind-forcing on fluid particle movement, experiments were conducted using wind stress time series estimated using

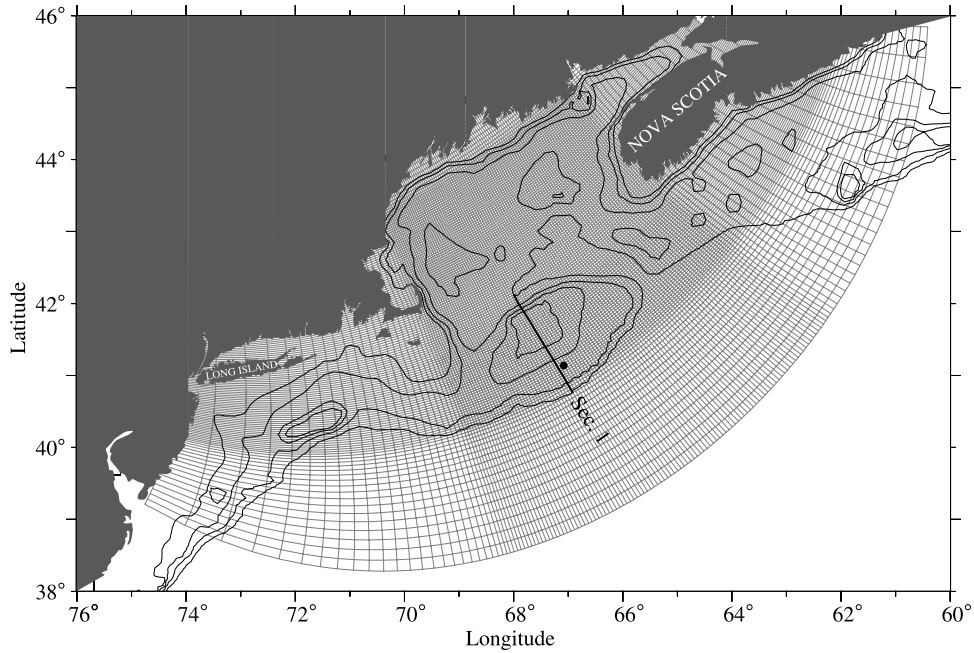


Figure 1. Bathymetry (in meters) of the New England, Gulf of Maine/Georges Bank, and Scotian continental margin with the numerical model grid superimposed. Heavy lines mark the three sections used to present the cross-bank distributions of temperature, salinity, and velocity. The solid circle on the southern flank of Georges Bank is the location of the meteorological mooring where data were collected during 1995.

moored meteorological measurements collected in 1995 on the southern flank of the Bank (Figure 2).

[10] The model was run as an initial value problem with bi-monthly averaged temperature and salinity fields for January–February, March–April, May–June, July–August, September–October, and November–December. Hydrographic fields were prepared by investigators at the Bedford Institute of Oceanography and were available from the Dartmouth College Ocean Modeling Group web site <http://www-nml.dartmouth.edu> [Naimie *et al.*, 1994; Naimie, 1996]. To facilitate comparison with the 2-D and 3-D model results presented by Chen and Beardsley [1998], Chen *et al.* [2001], and Loder *et al.* [1997], we also ran the model as an initial value problem with homogenous and vertically linear temperature conditions. In the latter case, the initial temperature varied from 15°C at the surface to 6°C at a depth of 300 m. The basic patterns found in this case were very similar to those in the bi-monthly case for May–June, so they were not included in the text.

[11] Fluid particles were tracked by solving the x , y , and z velocity equations

$$\frac{dx}{dt} = u, \quad \frac{dy}{dt} = v, \quad \frac{d\sigma}{dt} = \frac{\varpi}{H + \zeta}, \quad (1)$$

where u , v , and ϖ are the x , y , and σ velocity components. The relation between ϖ and w is defined as

$$\varpi = w - (2 + \sigma) \frac{d\zeta}{dt} - \sigma \frac{dH}{dt}, \quad (2)$$

where w is the vertical velocity in the z coordinate direction. Equations shown in (1) were integrated by means of a

fourth-order Runge-Kutta scheme with a truncation error of order $(\Delta t)^5$. Particle velocities used in this calculation were obtained using a bilinear interpolation from eight nearest grid points. At each time step, each particle was checked to see if it was located inside the numerical domain. If a particle hit the bottom, it was automatically removed from further consideration.

[12] The fourth-order Runge-Kutta method requires that the time step Δt satisfy the criterion $\Delta t K < 0.05$, where K is an upper bound of the spatial gradient of velocity. In our numerical experiments, K can be approximated by ω (the M_2 tidal frequency), which yields $\Delta t \omega \approx 0.029$ for $\Delta t = 207$ sec, which satisfies the above criterion. We tracked particles in the model space (x, y, σ) and then converted their trajectories back to the physical space (x, y, z) . This method avoids the interpolation errors due to repeated transformations from σ - to z -coordinate.

3. Bi-monthly Averaged Eulerian Residual Circulation

[13] In the model experiments started with the bi-monthly averaged temperature and salinity fields, the residual flow reached a quasi-steady state after about 10 model days, at which time the difference in residual flow over two subsequent tidal cycles was less than 0.5 cm/s in the absolute value and 0.7 cm/s in the standard deviation. Maps of surface-to-bottom density difference ($\Delta\sigma_{SB}$) (Figure 3) show the water to be vertically well mixed over GB in January–February and March–April. If we define the mixed region as the area of $\Delta\sigma_{SB} \leq 0.5$, this region becomes smaller and migrates toward the crest as stratification develops in May through August. A well-defined on-

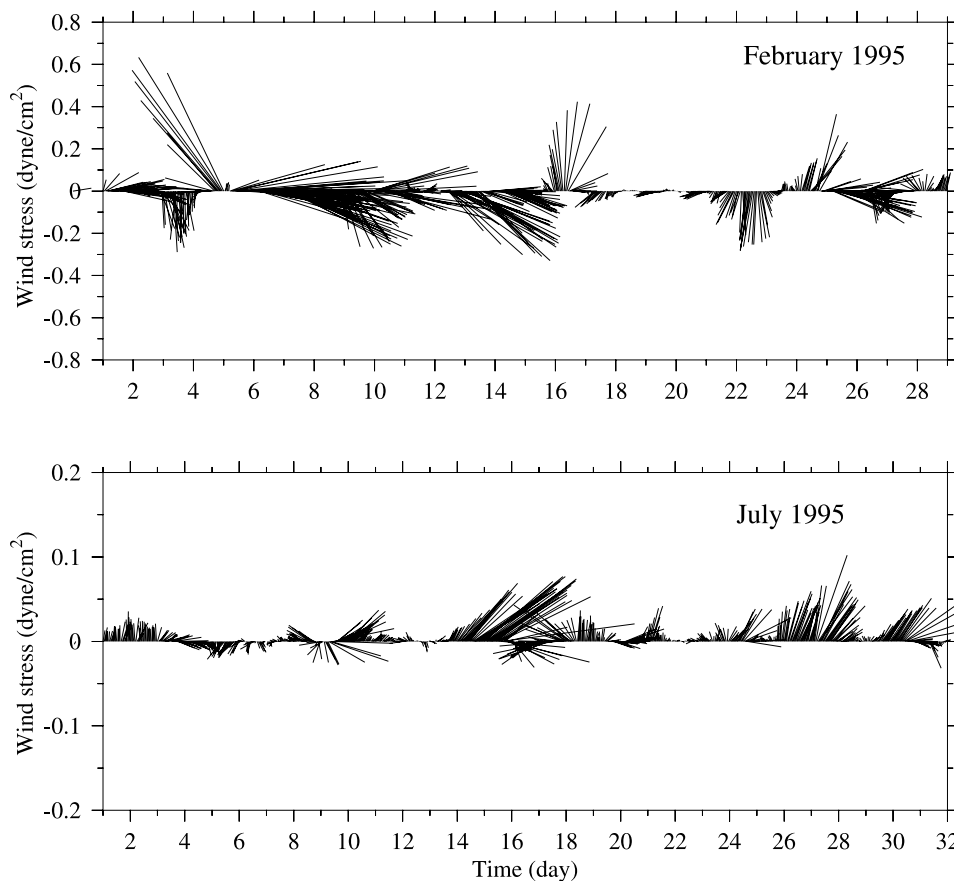


Figure 2. Wind stress time series during February and July 1995, estimated from wind and other measurements made at the southern flank-mooring site shown in Figure 1. The mean wind stress during these two months was 0.113 dyne/cm^2 and 0.014 dyne/cm^2 in amplitude and 108°N and 39°N in direction, respectively.

bank edge of the tidal mixing front is found around GB, located between the 50- to 60-m isobaths on the southern flank and near the 40-m isobath on the northern flank in July–August.

[14] The mean Eulerian residual flow field in these experiments was computed as the average over one tidal cycle after the initial 10 model day spin-up. As examples, in winter (January–February), two currents are dominant on GB (Figure 4, upper panel). The first is the tidally induced, topographically controlled clockwise residual circulation found around the crest of the bank, where a strong eastward/southeastward current jet of 15 to 18 cm/s forms along the edge of the northern flank and a relatively weaker and wider westward flow of 5 to 8 cm/s in the region shallower than 60 m on the southern flank. The second is a buoyancy-induced, westward mean current located near the 100-m isobath at the shelf break of the southern flank. These circulation patterns change only gradually from January through April. In summer (July–August), the clockwise residual circulation over the top of GB is significantly stronger as a result of the formation of the strong tidal mixing fronts over the northern and southern flanks (Figure 4, lower panel). The maximum velocity of the residual current reached 35 to 45 cm/s on the northwestern flank, 30 to 35 cm/s on the northern flank, and 5 to 10 cm/s on the southern flank. The residual flow on the southern

flank moved generally westward along the local isobaths, with several divergence and convergence zones between tidal and shelf-break fronts. Also, the surface currents tended to converge toward the tidal mixing front near the 50-m isobath and the shelf-break front near the 100-m isobath on the southern flank. The strong westward current found on the southern flank was due to the seasonal increase in stratification and the on-bank flows along the northwestern and northeastern flanks.

[15] The seasonal variation in the tidal mixing and shelf-break fronts and residual flow on GB were clearly illustrated in cross-bank distributions of temperature, salinity, and along-bank residual current (Figure 5). The tidal mixing front is characterized by strong temperature gradients, while the shelf-break front is dominated by persistent salinity gradients with the seasonal addition of the temperature field. In January–February, temperature and salinity were vertically well mixed on GB, with a weak salinity front at the northern edge and a relatively strong temperature/salinity front near the 80- to 90-m isobaths on the southern flank. In July–August, these two fronts intensified considerably and a cold core of shelf water formed near the bottom between tidal mixing and shelf-break fronts. Correspondingly, the January–February cross-bank section of Eulerian residual flow featured eastward flow along the northern edge and weaker westward flow over the southern flank.

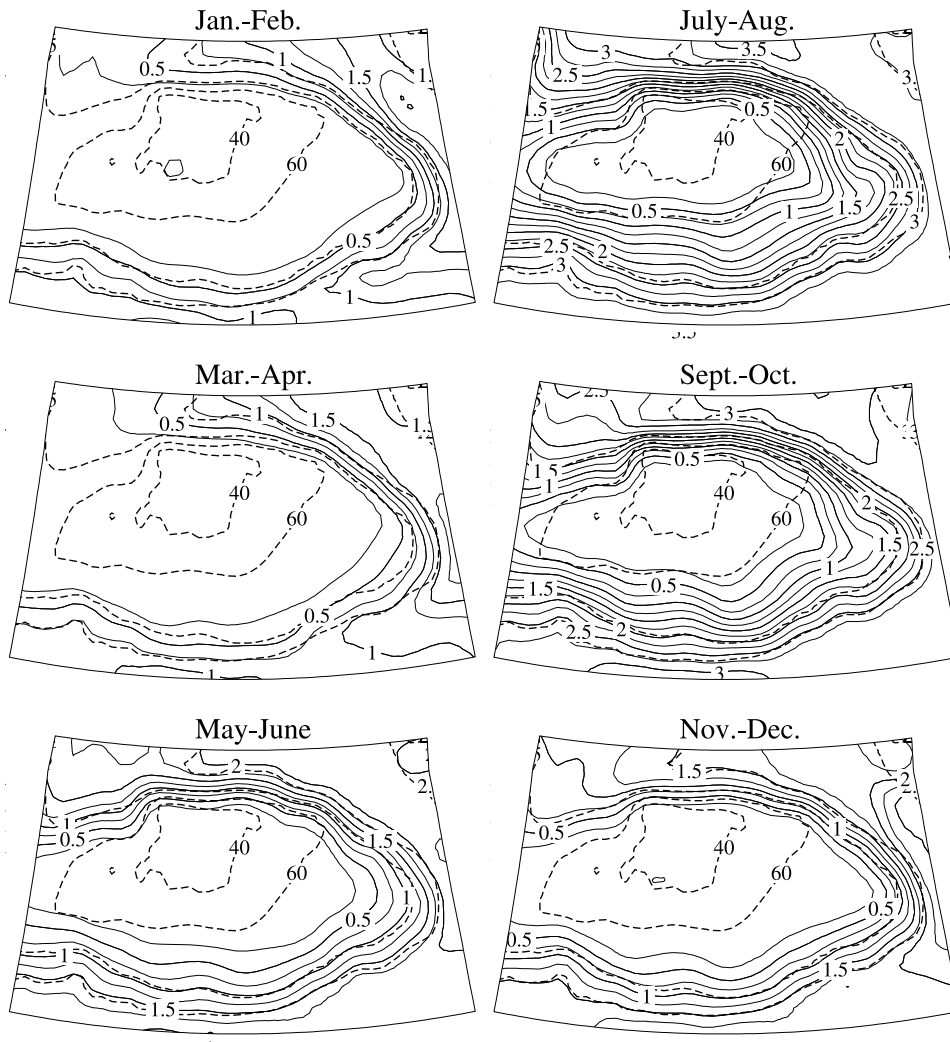


Figure 3. Bottom-surface density difference over Georges Bank found after model spin up for each bi-monthly initial stratification case from January–February to November–December. The contour interval is 0.25. The heavy dashed lines are the isobaths labeled 40, 60, 100, and 200 m from the top of the bank to the shelf break.

These flows became stronger during July–August. Two relatively high velocity cores were found over the southern flank in corresponding to tidal mixing and shelf-break fronts.

[16] Cross-bank sections of the mean Eulerian residual vertical current field featured a single circulation cell over the slope of the northern flank and multiple cells on the southern flank throughout the year (Figure 6). On the northern slope, the velocity field showed a convergent tendency toward the tidal mixing front near the surface, with a strong upward on-bank flow on the deep side and a weaker downward off-bank flow on the bank. This downward flow occurred near the bottom in all seasons, and tended to be recirculated upward in the upper 150 m off the bank. This circulation cell gradually intensified from winter to summer and then weakened again in fall. The maximum downward speed of the residual flow near the bottom increased from about 0.01 cm/s in January–February to 0.015 cm/s in July–August, occurring at depths of 50 and 100 m, respectively.

[17] On the southern flank, the wintertime circulation was mostly driven by tidal rectification in the mixed region and by buoyancy forcing at the shelf break. An upward velocity was found around the 30-m isobath, where the water depth decreased by about 20-m over a distance of 2 km. Apparent convergence zones existed near the surface between the 30- and 50-m isobaths in January–February. The relatively symmetric multiple circulation cells seen in July–August were consistent with the surface convergence and divergence flow pattern (as shown in Figure 4). An apparent near-surface convergence zone was also found at the shelf break, weakest in January–February and stronger in July–August. Downward flow occurred near the bottom of the slope at the shelf break in all seasons. The formation of multiple cells found on the southern flank of GB in summer seems to be caused by nonlinear wave interaction. By comparison of numerical results with analytical solutions derived by *Maas and Zimmerman* [1989a, 1989b], *Chen et al.* [1995] suggested that these multiple cells are caused by nonlinear interactions of barotropic and baroclinic waves

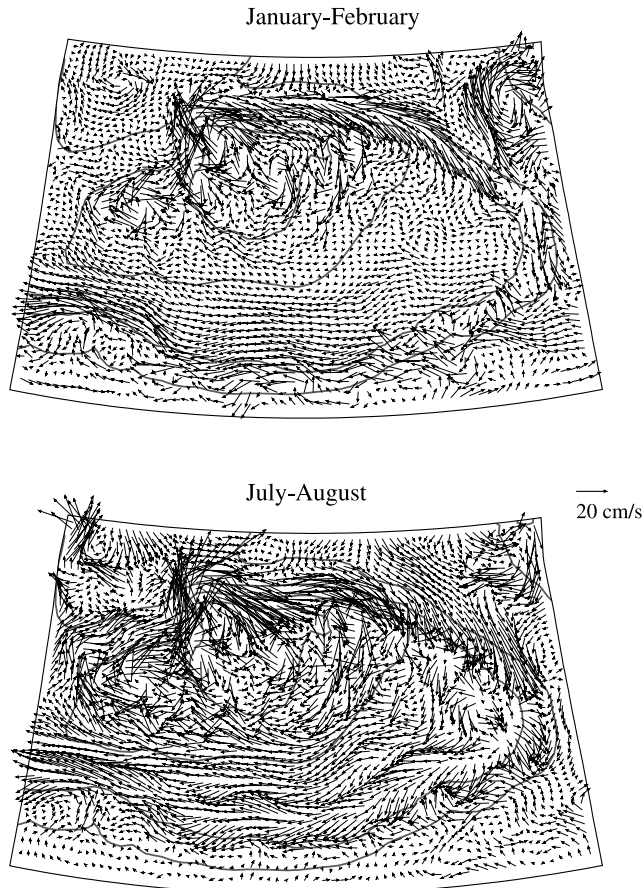


Figure 4. The surface residual Eulerian current field over Georges Bank found after spin up for the January–February and July–August bi-monthly averaged stratification cases. The heavy gray lines are the 40-, 60-, 100-, and 200-m depth contours, respectively.

over the small amplitude bottom topography. This suggestion also was supported by the example of the interaction of baroclinic and barotropic tidal currents shown by *Loder and Horne* [1991]. Both *Loder and Horne* [1991] and *Chen et al.*'s [1995] results show that the cross-bank scale of the cells is related to the baroclinic tidal wavelength.

[18] The 3-D Eulerian residual circulation patterns described above are in general consistent with previous modeling experiments conducted by *Naimie et al.* [1994] and *Naimie* [1996] using the Dartmouth finite element model with bi-monthly averaged stratification and by *Chen et al.* [2001] using the ECOM-si finite difference model with idealized summertime stratification. *Naimie et al.* [1994] and *Naimie* [1996] were the first to simulate the seasonal distribution of stratified residual flow in the Gulf of Maine/GB. A detailed discussion on the similarity between finite element and finite difference model results was given in *Chen et al.* [2001]. The cross-bank structure of our new 3-D model solutions (Figures 5 and 6) is predicted well by our earlier 2-D model experiments with idealized summertime stratification [*Chen et al.*, 1995; *Chen and Beardsley*, 1995]. Both 2-D and 3-D models show quite similar tidal-induced residual circulation patterns at the northern edge and on the southern flank,

indicative of the quasi-2-D nature of the flow over the center of the bank.

[19] It should be noted that our present model results show a more complex residual circulation over GB than that predicted by *Naimie* [1996], particularly in July–August when our model predicts multiple convergence and divergence regions between the tidal mixing and shelf-break fronts that do not appear in *Naimie*'s numerical solutions. Since the climatological conditions of temperature and salinity are the same in the ECOM-si and Dartmouth models and multiple secondary circulation cells also appear in our 2-D experiments with spatially smoothed topography, we believe that this difference in complexity is most likely due to the different advective numerical schemes used in the ECOM-si and Dartmouth models.

4. Residual Lagrangian Circulation and Stokes' Drift

[20] The residual Lagrangian velocity \vec{V}_L is defined here as the fluid particle velocity averaged over one tidal cycle. The Stokes' velocity \vec{V}_S is equal to the difference between the residual Lagrangian (\vec{V}_L) and Eulerian (\vec{V}_E) velocities, that is,

$$\vec{V}_L = \frac{\vec{X}_T - \vec{X}_o}{T}, \vec{V}_S = \vec{V}_L - \vec{V}_E, \quad (3)$$

where T is the M_2 tidal period, and \vec{X}_T and \vec{X}_o are the end and start positions of a particle over T . To calculate the Lagrangian current, we released a fluid particle at each grid point at the beginning of the second tidal cycle on the 10th model day (\vec{X}_o) and tracked this particle in the 4-D (x, y, σ, t) model solution for one tidal cycle to obtain \vec{X}_T . \vec{V}_L and \vec{V}_S were then computed using (3).

[21] The model results showed that the Eulerian and Lagrangian residual circulations differed significantly throughout the year (Figures 4 and 7). For example, in both January–February and July–August, at the surface on the northern and northeastern flanks, the Eulerian flow had a strong on-bank component while the Lagrangian current was more parallel to the local topography. Similar differences were found on the southern flank, where the Lagrangian currents were more closely aligned with the topography, especially between the tidal mixing and shelf-break fronts in summer. In July–August, the Lagrangian currents converged toward the outer edge of the tidal mixing front near the 60-m isobath.

[22] In both January–February and July–August, the surface Stokes' velocity \vec{V}_S varied with water depth, larger over the top of GB and along the entire northern edge of the bank (where tidal currents were strongest or the bottom slope steep) and smaller in the region deeper than 60 m on the southern flank where the bottom slope was smaller (Figure 8). On the top of GB, the Lagrange-Euler difference caused \vec{V}_S to be cyclonic, opposite in direction and comparable in magnitude to the Eulerian mean current \vec{V}_E . Here \vec{V}_S accounted for about 40% to 80% of \vec{V}_E , thus reducing the net Lagrangian flow. On the northeastern flank, especially during summer, \vec{V}_S was directed off-bank with speeds comparable to \vec{V}_E . Because of the cancellation between \vec{V}_S and \vec{V}_E , the Lagrangian current was more parallel to the

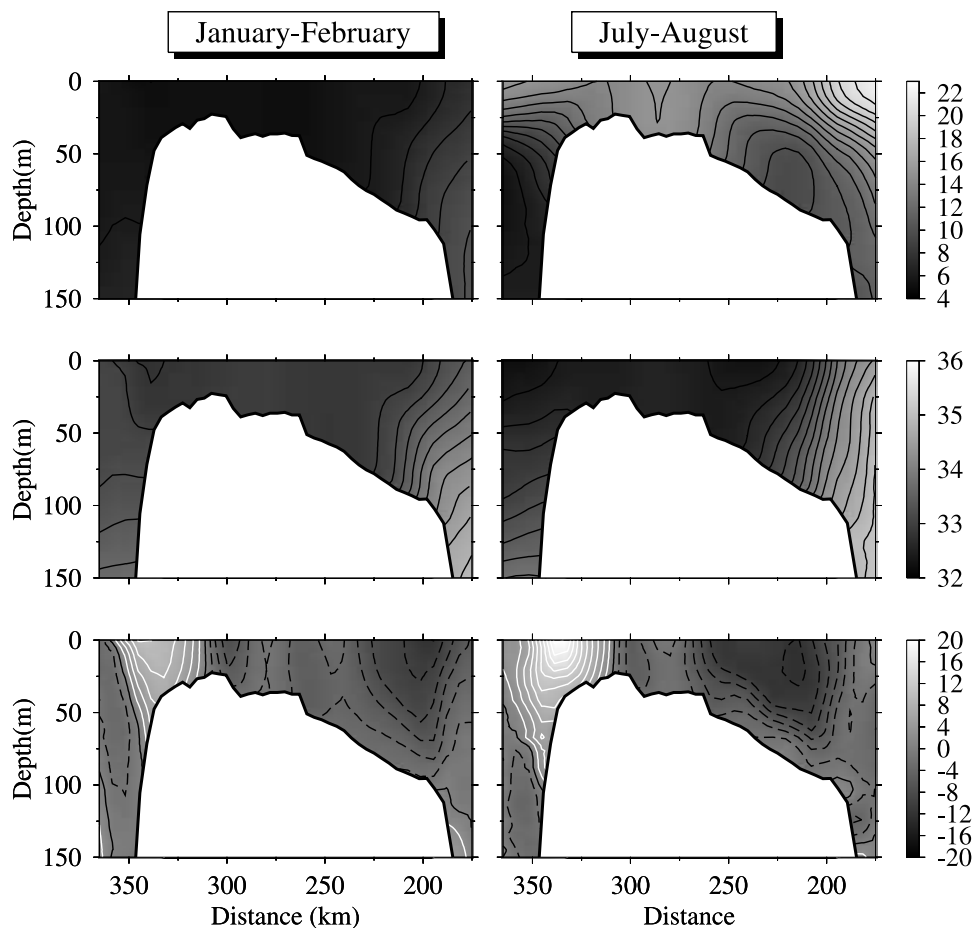


Figure 5. Cross-bank distribution of temperature (upper), salinity (middle), and along-bank current (lower) on section 1 (Figure 1) for the January–February and July–August bi-monthly averaged stratification cases. In the current plot, the solid lines denote eastward flow (into the page), and the dashed lines westward flow (out of the page). The contour intervals are 1.0°C , 0.2 , and 2.0 cm/s.

local topography and roughly 60–70% smaller than \vec{V}_E . On the southern flank, between tidal mixing and shelf-break fronts, \vec{V}_S exhibited multiple regions of divergence and convergence in the cross-bank direction. The cancellation between \vec{V}_S and \vec{V}_E caused relatively smoothed, along-isobath Lagrangian flow in that area. \vec{V}_E was generally smaller near the shelf-break where the tidal currents were weaker and the mean flow was dominated by the buoyancy-driven flow associated with the shelf-break front.

[23] The disparity in direction and magnitude between \vec{V}_L and \vec{V}_E was illustrated in cross-bank distributions of vertical velocity (Figures 6 and 9). In January–February and July–August, on the northern flank, \vec{V}_L showed strong upward flow over the bottom, which was opposite to the downward flow found in \vec{V}_E . \vec{V}_L exhibited two maximum upward velocities near the bottom: one near the 50-m isobath at the edge of the bank and the other near the 100-m isobath on the slope. The strong upward flow found off the bank in \vec{V}_E was replaced by a strong downward flow in \vec{V}_L , with maximum velocities at 60- to 70-m depths.

[24] On the southern flank, the Lagrangian and Eulerian residual vertical velocities were opposite near the 50-m isobath where there was a sharp change in the bottom slope. \vec{V}_L exhibited strong upward flow near the 50-m isobath,

with maximum vertical velocities at the bottom in January–February when the water was vertically and horizontally well mixed, and at the depth of 25 to 40 m below surface in July–August where large horizontal temperature and salinity gradients occurred. This upward flow intensified in summer and fall as a result of the formation of the tidal mixing front near the 50- to 60-m isobaths. Comparison of the cross-bank distributions of temperature (Figure 5) and Lagrangian vertical velocity (Figure 9) showed that the near-surface convergence zone in \vec{V}_L was on the stratified side of the tidal mixing front (about 5 km offbank from the inner edge of the front) in July–August and not at the edge of the front.

[25] Between the tidal mixing and shelf-break fronts, the difference between the vertical Lagrangian and Eulerian velocity fields was small in winter and early spring (January to April) (when the water was vertically and horizontally well mixed) but increased as seasonal stratification developed in late spring and summer and both fronts strengthen. For example, in July–August, multiple secondary circulation cells occurred in \vec{V}_E between these fronts, while these features almost disappeared in \vec{V}_L .

[26] By definition (3), \vec{V}_L and \vec{V}_E differed by \vec{V}_S . However, a physical explanation can be given for the model

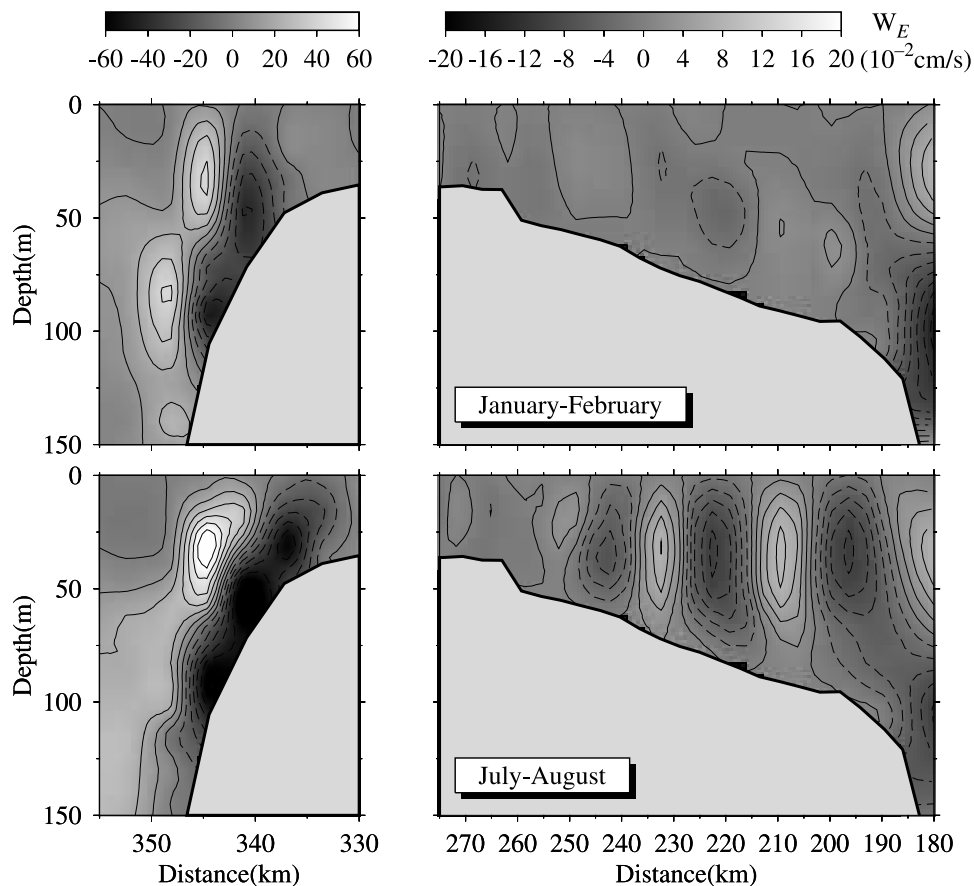


Figure 6. Cross-bank distribution of residual Eulerian vertical velocity along the northern flank (left) and southern flank (right) elements of section 1 for the January–February and July–August bi-monthly averaged stratification cases. Solid lines denote upward flow and dashed downward flow. The contour interval is 10×10^{-2} cm/s for the northern flank and 2.0×10^{-2} cm/s for the southern flank.

Stokes’ drift, which is caused by the spatial difference in amplitude and phase of cross-bank tidal velocity over the steep bottom slope [Loder *et al.*, 1997]. In winter, the top and flanks of the bank are essentially un-stratified. The sharp change in the barotropic cross-bank tidal flow over steep topography produces a strong nonlinear interaction between the along- and cross-bank components of the tidal current. This generates a strong Stokes’ drift over the northern flank and near the 50-m isobath on the southern flank [Loder *et al.*, 1997; Chen and Beardsley, 1998]. The vertical component of this Stokes’s drift is generally larger than the Eulerian component, causing the Lagrangian vertical flow to oppose the Eulerian flow (Figure 10).

[27] As stratification increased in spring and summer, internal tidal flow develops on both northern and southern flanks [Chen *et al.*, 1995], which tends to enhance the nonlinear interaction between tidal currents and produces a stronger Stokes’ drift. This summertime intensification of \vec{V}_S results in a stronger upslope residual Lagrangian flow on the northern flank and weakened secondary Eulerian circulation cells in the stratified region between the tidal mixing and shelf-break fronts on the southern flank. Similar features are evident on the northeastern and northwestern flanks, where relatively strong Lagrangian upward flow occurs near the bottom in opposition to the vertical Eulerian velocity, implying that this is a general feature around the

northeastern-northern-northwestern flanks of GB. Multiple Stokes velocity cells on the southern flank are very similar to those found by Loder and Horne [1991], which is believed to be caused by the nonlinear interaction of barotropic and baroclinic tidal currents.

5. Tidal- and Wind-Forced Particle Motion

[28] To investigate the influence of tidal and wind-forcing on particle motion, we conducted particle tracking experiments using three external forcing functions: tide only, tide plus mean wind stress, and tide plus time-dependent wind stress. Particles were released at each grid point at the beginning of the 11th model day and tracked for one month in two bi-monthly stratification cases, July–August and January–February. The wind stress time series used here was estimated using moored meteorological measurements made on the southern flank during 1995 and the TOGA/COARE bulk parameterizations [Beardsley *et al.*, 2002]. The wind stress was averaged over each bi-monthly period to obtain the mean wind stress for that case. The wind stress was assumed to be uniform in space.

5.1. July–August Case

[29] Trajectories of particles released at the first σ -level (“near-surface”) and the σ -level closest to the bottom

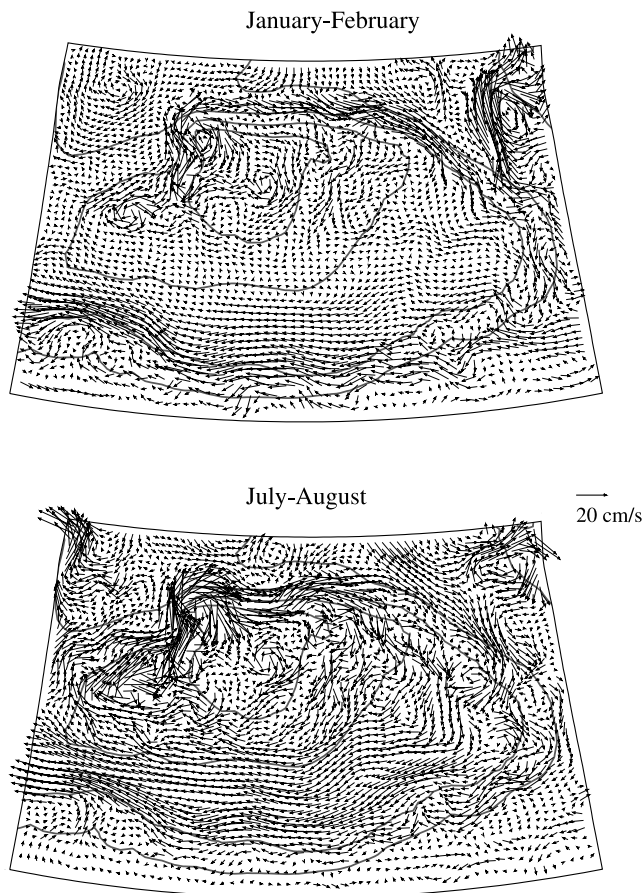


Figure 7. The surface residual Lagrangian current field over Georges Bank for the January–February and July–August bi-monthly averaged stratification cases. The heavy gray lines are the 40-, 60-, 100- and 200-m depth contours, respectively.

(“near-bottom”) are shown in Figure 11. With only tidal forcing, the near-surface particles tend to move clockwise around GB, with speeds of 30 to 40 cm/s on the northwestern edge, 25 to 30 cm/s on the northern edge, and 2 to 10 cm/s near the tidal mixing and shelf-break fronts on the southern flank. The clockwise movement back to the southern flank occurred via three primary paths: (1) along the northwestern edge where the bottom topography varies sharply in both along- and cross-bank directions; (2) between the 50- to 60-m isobaths along the tidal mixing front; and (3) along the 100-m isobath at the outer edge of the bank. These three paths are very similar to the drifter trajectories observed by *Limeburner and Beardsley* [1996]. There was no significant cross-frontal particle movement near the surface, except at the northwestern edge where particles are carried southeastward onto the bank as a small-scale clockwise gyre.

[30] The basic pattern of the near-bottom particle trajectories is similar to that observed near the surface, except on the northeastern slope where particles tended to move westward along the bank. On the southern flank, the near-bottom trajectories originating between the 60- and 70-m isobaths in the stratified region and near the 40-m isobath in the mixed region converged toward the tidal mixing front

around the 45- to 50-m isobaths (Figures 12 and 13). A second convergence zone was seen near the 80-m isobath in the shelf-break front, where particles over the outer shelf up to the 70-m isobath moved toward the base of the front and then upward in the front (Figure 13). This indicates that the near-bottom particle motion was divergent between the tidal mixing and shelf-break fronts on the southern flank. Further examination of other particle trajectories on the southern flank showed that the location of this divergence zone varied along the bank in association with the along-bank location of the shelf-break front.

[31] On the northern flank, remarkable on-bank flows occurred at the northwestern and northern edges. Particles released near the bottom tended to move upward on their eastward along-bank journey. For example, a particle released near the bottom at a depth of 155 m moved up to 20 m below the surface over 14 tidal cycles (about 7 days) before it left the northern flank (Figure 14). Similar trajectories were found in the rest area of the northern flank, which were consistent with our earlier finding that the Lagrangian velocity generally opposed the Eulerian velocity on the northern flank.

[32] The effects of wind-forcing on the near-surface particle motion on GB varies with water depth, being more

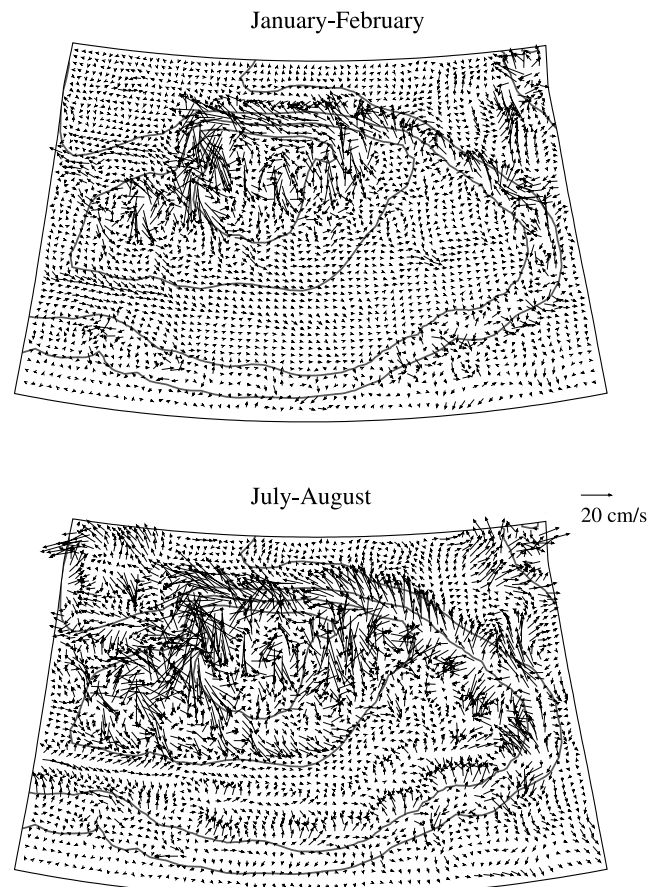


Figure 8. The surface residual Stokes' drift velocity over Georges Bank for the January–February and July–August bi-monthly averaged stratification cases. The heavy gray lines are the 40-, 60-, 100-, and 200-m depth contours, respectively.

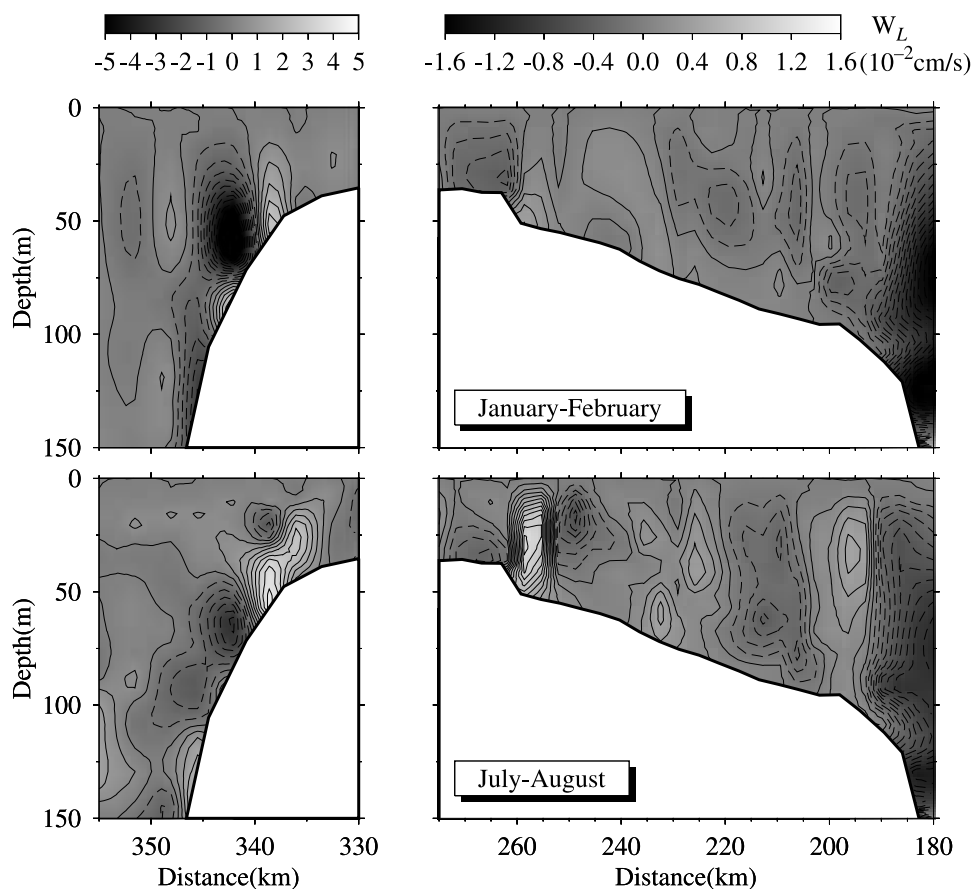


Figure 9. Cross-bank distribution of the residual Lagrangian vertical velocity along section 1 for the January–February and July–August bi-monthly averaged stratification cases. Solid lines denote upward flow, dashed lines downward flow. The contour interval is 0.5×10^{-2} cm/s for the northern flank and 0.1×10^{-2} cm/s for the southern flank.

important in deeper water where tidal forcing is relatively weaker. In the case with tidal and mean wind stress ($|\vec{\tau}_s| = 0.014$ dyne/cm² with a northeastward direction) forcing, the near-surface clockwise particle motion seemed to intensify significantly, especially on the northeastern flank where the small-scale eddy-like particle trajectories were replaced by more-organized along-isobath motion (Figure 11b). The addition of mean wind-forcing enhanced the near-surface convergence toward the shelf-break front and caused an off-bank movement near the surface at the shelf break off the 100-m isobath. No significant near-surface cross-frontal particle movement was found near the tidal mixing front in the case with mean wind stress forcing.

[33] In the case with tidal and time-dependent wind stress forcing (Figure 11c), the near-surface particle trajectories were more complex but the basic pattern of clockwise motion remains unchanged. The time-varying wind stress led to significant off-bank Ekman transport on the outer shelf of the southern flank, which was more evident than in the case with mean wind-forcing even though the total momentum input for both cases were the same. Both mean and time-dependent wind stress had relatively little influence on particle movement near the bottom since the near-bottom particle trajectories remain almost unchanged in the three cases (Figure 11c).

[34] Comparisons of selected particle trajectories for the three forcing cases are shown in Figure 15. At the north-western edge, the near-surface particles tended to move onto the center of the bank with tide only and tide plus mean wind-forcing, but were carried eastward along the bank with time-dependent wind-forcing. Near-surface particles starting at the 60-m isobath on the northern flank moved eastward along the 100-m isobath, then turned on-bank to move along the 60-m isobath with tide only and tide plus mean wind-forcing. The same particles turned on-bank earlier and moved southward between the 40- and 60-m isobaths with time-dependent wind stress forcing. At the center of the bank, the near-surface particles moved westward, then northward and northeastward to flow along the bank with tide only forcing. These particles were trapped in the center within the 40-m isobath with the addition of mean wind-forcing. Time-dependent wind-forcing caused these same particles to move southward and southwestward toward the tidal mixing front near the 60-m isobath. On the southern flank, the near-surface particles starting at the 40-m isobath in all three forcing cases moved westward and then northeastward along the bank, with the particles with time-dependent wind stress forcing crossing the tidal mixing front onto the center of the bank. For the spatially uniform wind stress fields used here, only the near-surface particle

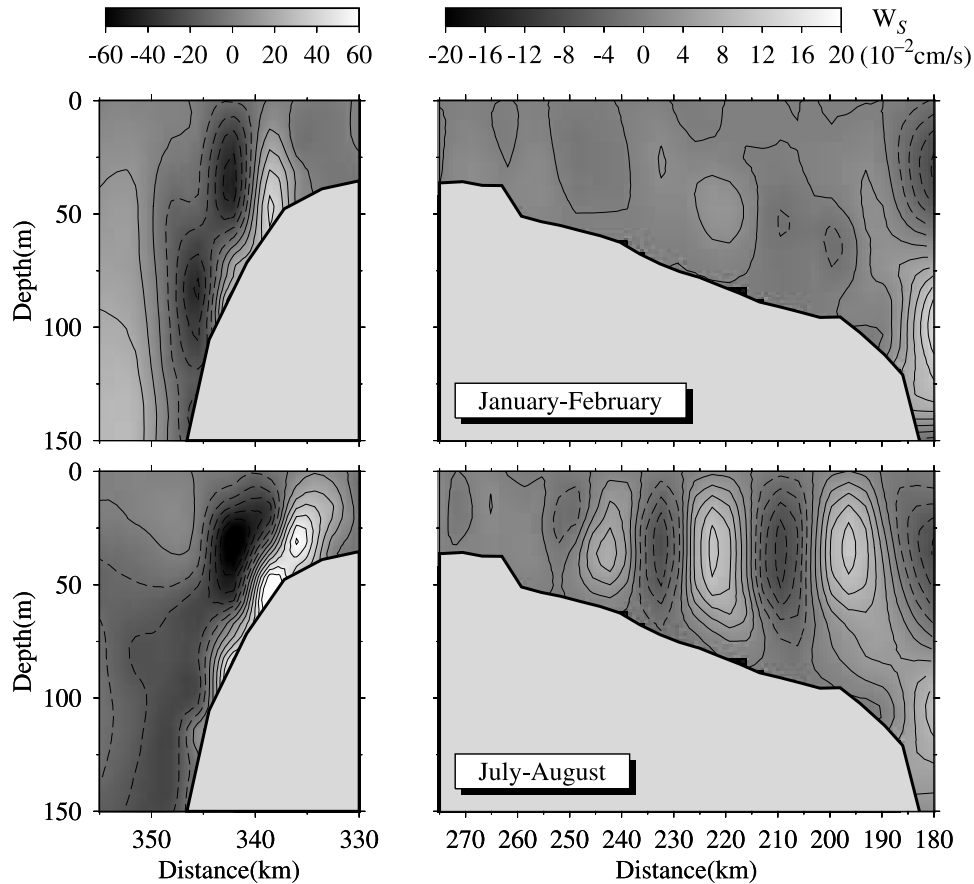


Figure 10. Cross-bank distribution of residual Stokes' vertical velocity along section 1 for the January–February and July–August bi-monthly averaged stratification cases. Solid lines denote upward flow, dashed downward flow. The contour interval is 10×10^{-2} cm/s for the northern flank and 2.0×10^{-2} cm/s for the southern flank.

movement over the center and eastern side of the outer southern flank exhibited significant wind-induced off-bank movement. Over the western side of the outer southern flank, the near-surface particle movement was due primarily to tidal forcing. The addition of wind-forcing to summer stratification modifies only slightly the speed and direction (and thus movement) of near-bottom particles. This indicated that the near-bottom cross-frontal particle motion was due mainly to tidal forcing, as suggested by earlier 2-D model results [Chen and Beardsley, 1998].

5.2. January–February Case

[35] In January–February, near-surface particles tended to move clockwise around GB and westward over the outer shelf on the southern flank (Figure 16) only in the case of tide forcing only. The addition of the mean southeastward ($|\bar{\tau}_s| = 0.011$ dyne/cm²) or the time-dependent wind stress changed the particle motion significantly. The closed nature of the clockwise Lagrangian flow on GB shown in Figure 16a disappeared, and instead, the near-surface particles tended to be carried off-bank (“washed off”) along the center and western regions of the outer southern flank. The near-surface particle trajectories were more complex with time varying wind stress. Unlike July–August, episodic cold fronts and coastal lows frequently moved over GB in January–February, causing large wind stress fluctuations.

On the other hand, the addition of wind-forcing caused little change in the near-bottom particle movement. Thus wind-driven on/off-bank particle movement occurred primarily through the surface Ekman transport in the climatological winter mean condition with no storm passages.

[36] The tidal mixing front was absent on the southern flank of the bank due to the lack of vertical stratification in the January–February density field. The shelf-break front was weaker during that period and located off-bank from its July–August position. Thus in January–February, the particle trajectories exhibited only a weak convergence near the bottom at the on-bank edge of the shelf-break front on the southern flank. On the northern flank, the winter near-bottom particle trajectories were similar to those found in summer, that is, the particles tended to move upslope in opposition to the downslope Eulerian residual flow there.

6. Passive Tracer Experiments

[37] In the case with July–August stratification, near-bottom particles tended to move toward the tidal mixing and shelf-break fronts on the southern flank. Some particles even moved across the tidal mixing front near the bottom, suggesting cross-frontal water transport between crest and southern flank. The particle tracking experiments provided us insight into the basic Lagrangian kinematics but did not

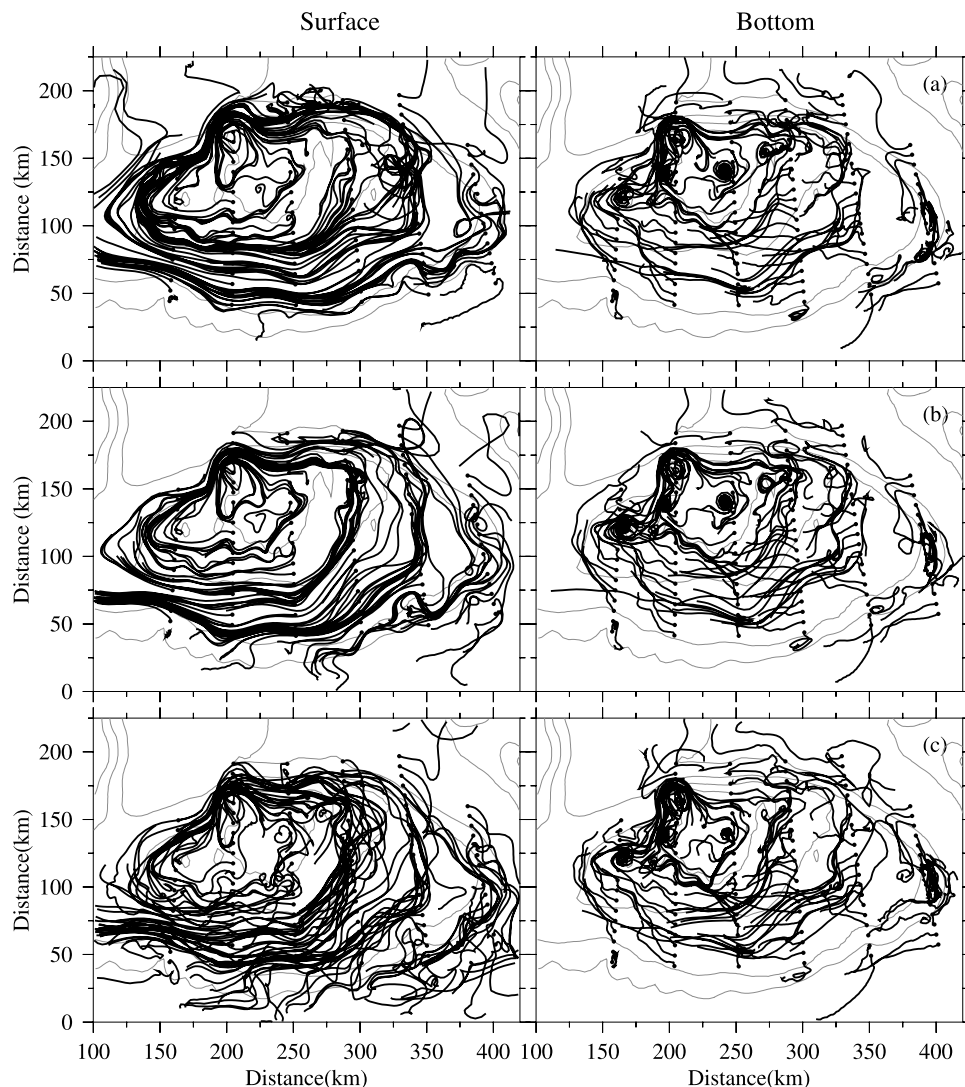


Figure 11. The near-surface (left) and near-bottom (right) trajectories of particles over Georges Bank for the three cases with only tide forcing (upper), tide plus mean wind-forcing (middle) and tide plus time-dependent wind-forcing (lower). Each dot indicates the initial location of a particle. The particles were released in the July–August stratified flow field at the end of the 10th model day and followed for 30 days.

include the effect of diffusion. To examine the influences of pure motion (advection) and diffusion on the cross-frontal transport of nutrients, we conducted passive tracer experiments with and without diffusion. To reduce numerical artifacts associated with either simple upwind or central difference schemes, we used the Multidimensional Positive Definite Advection Transport Algorithm (MPDATA) introduced by *Smolarkiewicz* [1984]. The basic concept of MPDATA is the successive application of an upwind scheme with a correction to the first-order truncation error using an “anti-diffusion” velocity. The repeated procedure yields a positive definite advection algorithm with second-order accuracy [*Smolarkiewicz and Clark, 1986; Smolarkiewicz and Grabowski, 1990*].

[38] The passive tracer P with concentration of 1 was placed in an area around the tidal mixing front at the end of the 10th model day when the residual current reached a quasi-steady state in the case with July–August stratifica-

tion and tidal forcing only (Figure 17a). The vertical thickness of the initial tracer layer was 20 m above the bottom on the southern flank but varied on the northern flank. The tracer was then tracked over 30 model days for the cases with (1) pure advection, (2) advection plus vertical diffusion, and (3) advection plus vertical and horizontal diffusion. The vertical diffusion was computed directly using the MY level 2.5 turbulent closure model and a constant horizontal diffusivity of $20 \text{ m}^2/\text{s}$ was used in our numerical experiments. Our description of the tracer movement focused on the northern and southern flanks and the total cross-frontal exchange was estimated around the tidal mixing front over the bank.

[39] In the case with pure advection, the tracer spread both on- and off-bank and upward over the bank (Figure 17). At the end of the 5th day, the tracer was still concentrated over the slope on the northern flank, and to a lesser extent, at a few locations around the bank. On the southern flank,

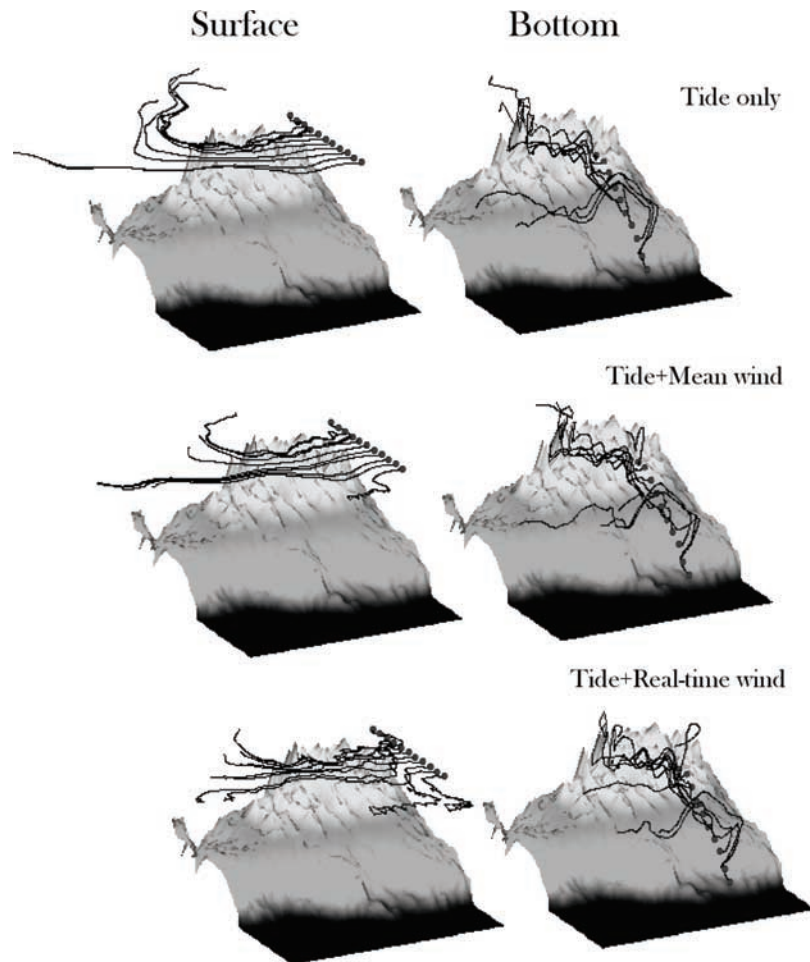


Figure 12. A 3-D view of selected particle trajectories near the surface and bottom on the southern flank of Georges Bank for the three cases shown in Figure 11. The dots show the initial locations of the particles. The particles were tracked for 30 days.

the tracer had two cores of maximum concentration near the bottom: one near the tidal mixing front around the 60-m isobath and the other near the inshore boundary of the shelf-break front around the 85-m isobath. This pattern was consistent with a near-bottom divergence zone located between the tidal mixing and shelf-break fronts, as suggested by the Lagrangian particle tracking results.

[40] When vertical diffusion was added, the tracer was spread rapidly upward over much of the bank with little change in the vertical integrated tracer concentration (Figure 18, left). This resulted in smaller near-bottom concentrations, especially noticeable on the southern flank. The addition of horizontal diffusion tended to spread out or eliminate the near-bottom maximum concentration cores (Figure 18, right).

[41] To illustrate the flow of tracer across the front, we considered a control volume covering the top of the bank and surrounded by the boundary of the tidal mixing front, and computed the amount of tracer found within the control volume as a function of time (i.e., if CT is the amount of tracer released initially and CV is the amount of tracer found within the control volume at time t , then $100 \times CV/CT$ is the percent tracer in the control volume at that time). Figure 19 shows that the amount of tracer within this control volume

increased quickly initially and then more slowly with time. In the case with pure advection, the amount reached 20% on model day 30 after the tracer was released, but it dropped to 12% when vertical diffusion was included, and to 15% with both vertical and horizontal diffusion. This suggests that vertical diffusion tends to reduce cross-frontal transport and its effects can cause a decrease of roughly 40% in the total amount of tracer that crosses the tidal mixing front. On the other hand, horizontal diffusion tends to enhance cross-frontal transport and its contribution should depend on the value of the horizontal diffusion coefficient. In these model experiments, the horizontal diffusivity was $20 \text{ m}^2/\text{s}$, and the contribution of horizontal diffusion to the cross-frontal tracer volume could reach 15%.

[42] As shown in the particle tracking experiments, the addition of wind-forcing in summer caused little change in the near-bottom particle motion over GB. Thus there should be little change in the near-bottom cross-frontal flux of tracer due to wind-forcing, which was shown in Figure 19b.

7. An Analytical Particle Tracking Model

[43] We note here that the particle velocity used in our 3-D Lagrangian particle tracking experiments was calcu-

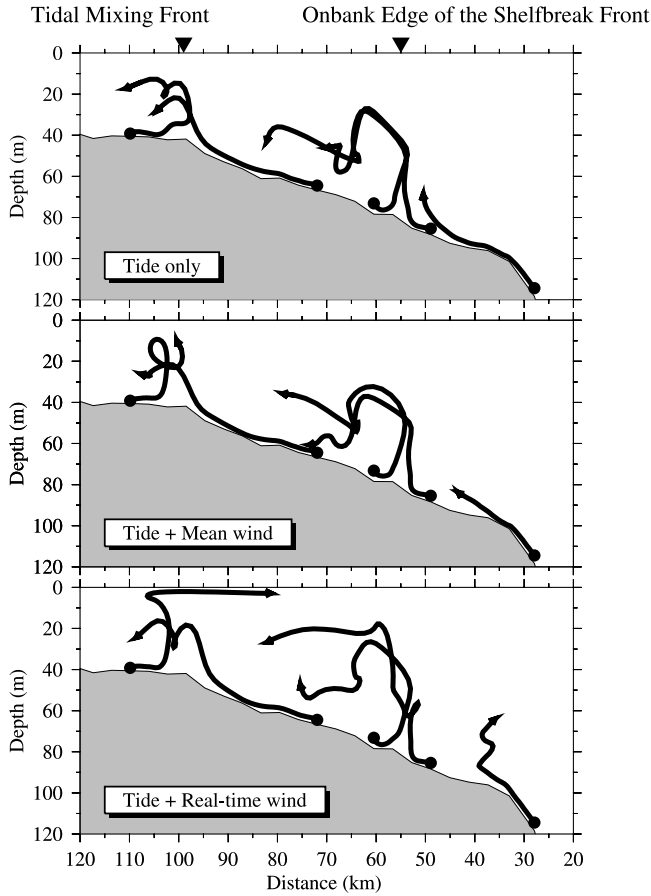


Figure 13. A 2-D view of selected near-bottom particle trajectories in the cross-bank direction on the southern flank of Georges Bank for the three cases shown in Figure 11. The dots denote the initial positions of the particles. The particles are tracked for 30 days.

lated using a bilinear interpolation from the eight nearest grid points in the curvilinear σ -coordinate system. The interpolation errors depend on horizontal and vertical resolution, which theoretically can be made smaller using higher grid resolution. Since the vertical velocity was normally one or two orders of magnitude smaller than the horizontal velocity, interpolation errors in the vertical was probably more critical, particularly over regions of steep bottom slope like the northern flank of GB. To check if our model results based on particle tracking were robust, we reran some experiments using 61 σ -levels and found quite similar results. As in the original 31 σ -level experiments, the tide-induced Lagrangian and Eulerian residual flows were in opposite directions over the steep northern slope. To further test this result, we developed the following idealized model to examine Lagrangian particle motion over steep topography and applied this model to the northern flank of GB.

[44] The basic character of the cross-bank current on the northern flank can be captured by a sum of tidal and residual currents as expressed in the stream function

$$\psi = \psi_T + \psi_R = -\frac{H_d U_d}{H(x)} z \sin \omega t + A_o \left(1 - e^{-\frac{z+H(x)}{z_B}}\right) \sin \frac{\pi z}{H(x)} \sin \frac{2\pi x}{L}, \quad (4)$$

where x and z are Cartesian coordinates, positive on-bank and upward (see Figure 20); ψ_T and ψ_R are the stream functions for tidal and residual currents, respectively; H_d the water depth off the bank; U_d the vertically averaged tidal current velocity off the bank; $H(x)$ the water depth; ω the M_2 tidal frequency; A_o the magnitude of the residual stream function; L the horizontal scale of the residual circulation cell; and z_B the thickness of the bottom boundary layer.

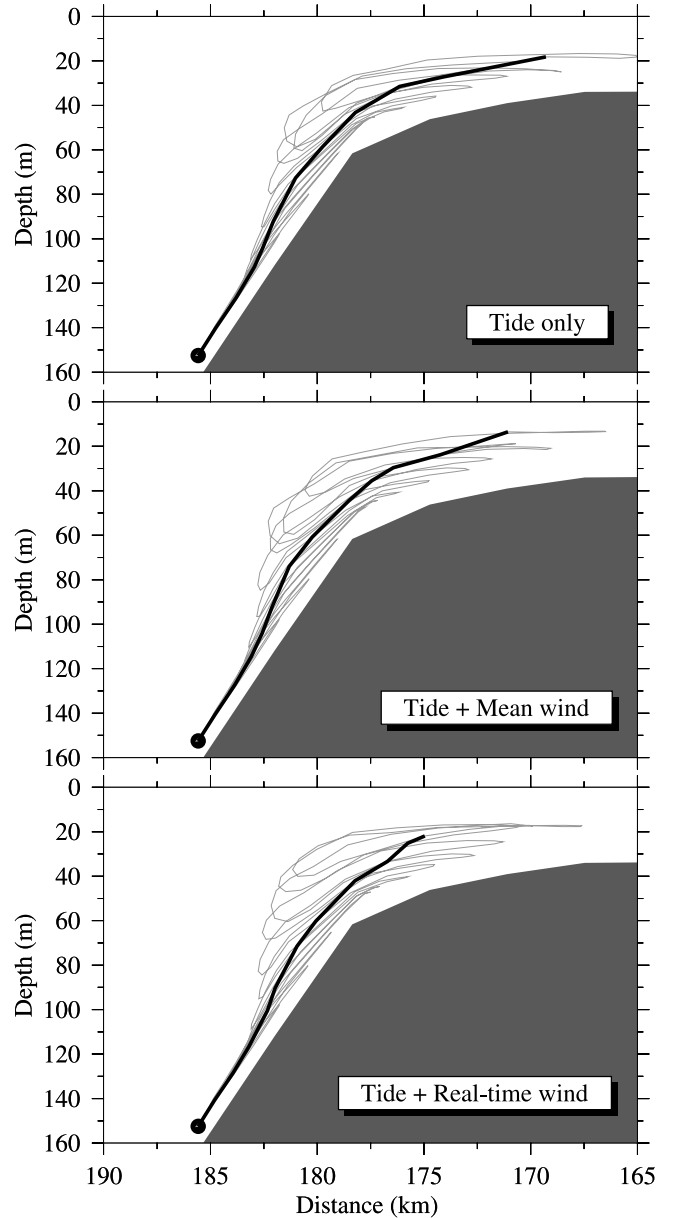


Figure 14. A 2-D view of selected near-bottom particle trajectories in the cross-bank direction on the northern (section 1) flank of Georges Bank for the three cases shown in Figure 11. The thin gray solid lines show the particle paths plotted hourly and the thick black lines show the residual particle motion (averaged over a tidal cycle). The dot shows the initial position of the particle.

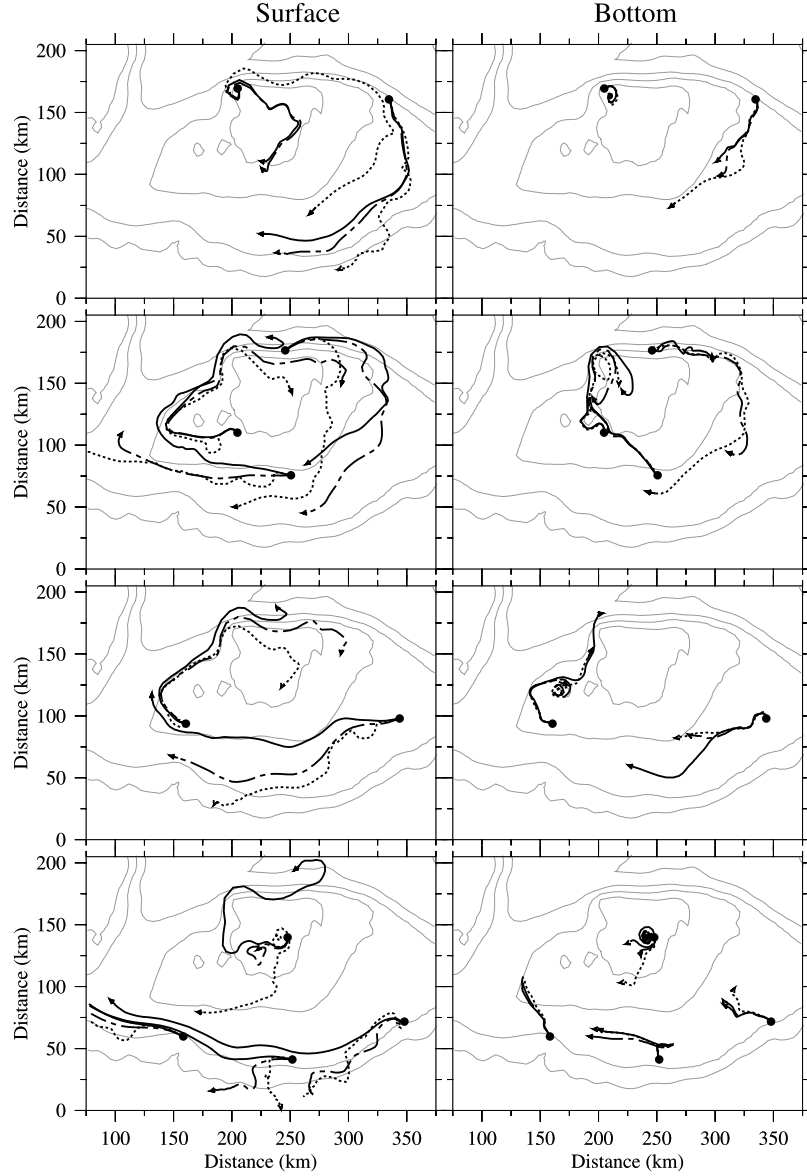


Figure 15. Trajectories of selected particles released near the surface (left) and bottom (right) for the three cases shown in Figure 11. Solid lines are particle paths with tide only forcing, semidashed lines with tide and mean wind-forcing, and the dashed lines with tide and time-dependent wind-forcing. Dots are the initial locations of particles, and thin solid lines are the 40-, 60-, 100-, and 200-m depth contours.

[45] For an incompressible fluid and nondivergent flow, the horizontal and vertical velocities can be expressed using the stream function as

$$u = \frac{dx}{dt} = -\frac{\partial\psi}{\partial z} = \frac{H_d U_d}{H(x)} \sin \omega t + \hat{U}_R \left[\frac{H(x)}{z_B \pi} e^{-\frac{z+H(x)}{z_B}} \sin \frac{\pi z}{H(x)} + (1 - e^{-\frac{z+H(x)}{z_B}}) \cos \frac{\pi z}{H(x)} \right] \sin \frac{2\pi x}{L} \quad (5)$$

$$w = \frac{dz}{dt} = \frac{\partial\psi}{\partial x} = \frac{H_d U_d}{H^2(x)} \alpha z \sin \omega t + \hat{W}_R \alpha \left[\frac{L}{z_B \pi} e^{-\frac{z+H(x)}{z_B}} \sin \frac{\pi z}{H(x)} - \frac{L}{H^2(x)} \left(1 - e^{-\frac{z+H(x)}{z_B}} \right) \cos \frac{\pi z}{H(x)} \right] \cdot \sin \frac{2\pi x}{L} + 2\hat{W}_R \left(1 - e^{-\frac{z+H(x)}{z_B}} \right) \sin \frac{\pi z}{H(x)} \cos \frac{2\pi x}{L} \quad (6)$$

where $\hat{U}_R = A_o \pi / H(x)$; $\hat{W}_R = \hat{U}_R H(x) / L$; $\alpha = dH(x)/dx$.

[46] The bottom depth is specified as a cosine function over the slope linking constant values on top of and off the bank, with the form of

$$H(x) = \begin{cases} H_s & x \geq 0 \\ 0.5(H_d + H_s) & -L_s < x < 0 \\ -0.5(H_d - H_s) \cos \frac{\pi}{L_s} (x + L_s) & -L_s < x < 0 \\ H_d & x \leq -L_s \end{cases} \quad (7)$$

where $H_s = 40$ m, $H_d = 300$ m, and L_s is the width of the slope.

[47] In this flow field, the tidal current is characterized by a barotropic periodic motion with a cross-slope volume flux that varies only in time, while the residual flow is given by a double cell circulation with relatively strong downwelling in the bottom boundary on the upper slope. Particles were released near the bottom on the slope and tracked using the

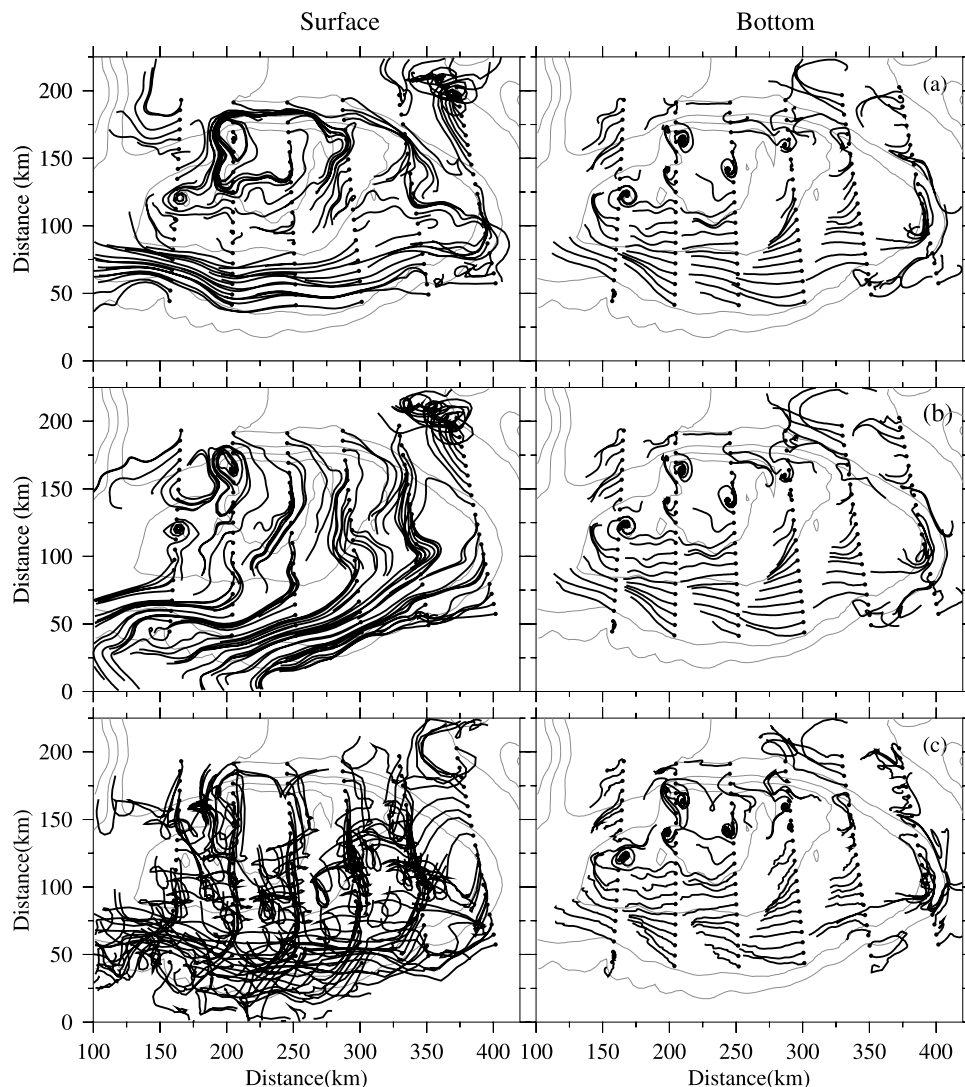


Figure 16. Near-surface (left) and near-bottom (right) trajectories of particles over Georges Bank for the three cases with tide only forcing (upper), tide plus mean wind-forcing (middle) and tide plus time-dependent wind-forcing (lower). Each dot indicates the initial location of a particle. The particles were released in the January–February stratified flow field at the end of the 10th model day and followed for 30 days.

fourth-order Runge-Kutta method with a time step of 6.0 sec (6480 time steps for a tidal cycle). The model was run for cases with different bottom slope (i.e., with different L_s) using the following tidal and residual flow fields based on the 3-D model results for the northern flank of GB: $U_d = 16$ cm/s, which produced a tidal velocity of 120 cm/s at the 40-m isobath on the top of the bank; $A_o = 1.6$, which gives a maximum cross-bank residual velocity of 8.2 cm/s near the bottom at the 60-m isobath; and z_B equal 1 m.

[48] Figure 21 shows the residual movement of particles tracked over 10 tidal cycles for two cases, $L_s = 20$ km (bottom slope $\alpha = 0.013$) and 10 km ($\alpha = 0.026$) respectively, in which L equals L_s to ensure the slope contains similar two double-cell circulation patterns for the two cases. In the first case with no tidal component, particles move clockwise following the streamlines of the steady Eulerian residual flow, with downward flow near the bottom on the slope. When the tidal current is added, particles still

tend to move clockwise but with reduced speed and different paths. In case two with steeper bottom slope, the particles near the bottom reverse and move *upslope* in the opposite direction to the Eulerian residual velocity. This result suggests that for a given flow field, the slope of the bottom topography has a critical impact on the particle movement. On the northern flank of GB, the bottom slope is about 0.025 or larger, comparable to that used in our second case. This supports the idea that the near-bottom particle motion can oppose the Eulerian residual flow on the northern flank of GB.

[49] Additional experiments with this idealized model show that the direction of particle motion is related also to the thickness of the slope bottom boundary layer and strength of the tidal flow. For a given flow field (U_d , A_o , L , L_s), as z_B increases, the particles near the top of the bottom boundary layer tend to reverse sooner than particles near the bottom. This tendency does not occur when U_s (the cross-isobath tidal

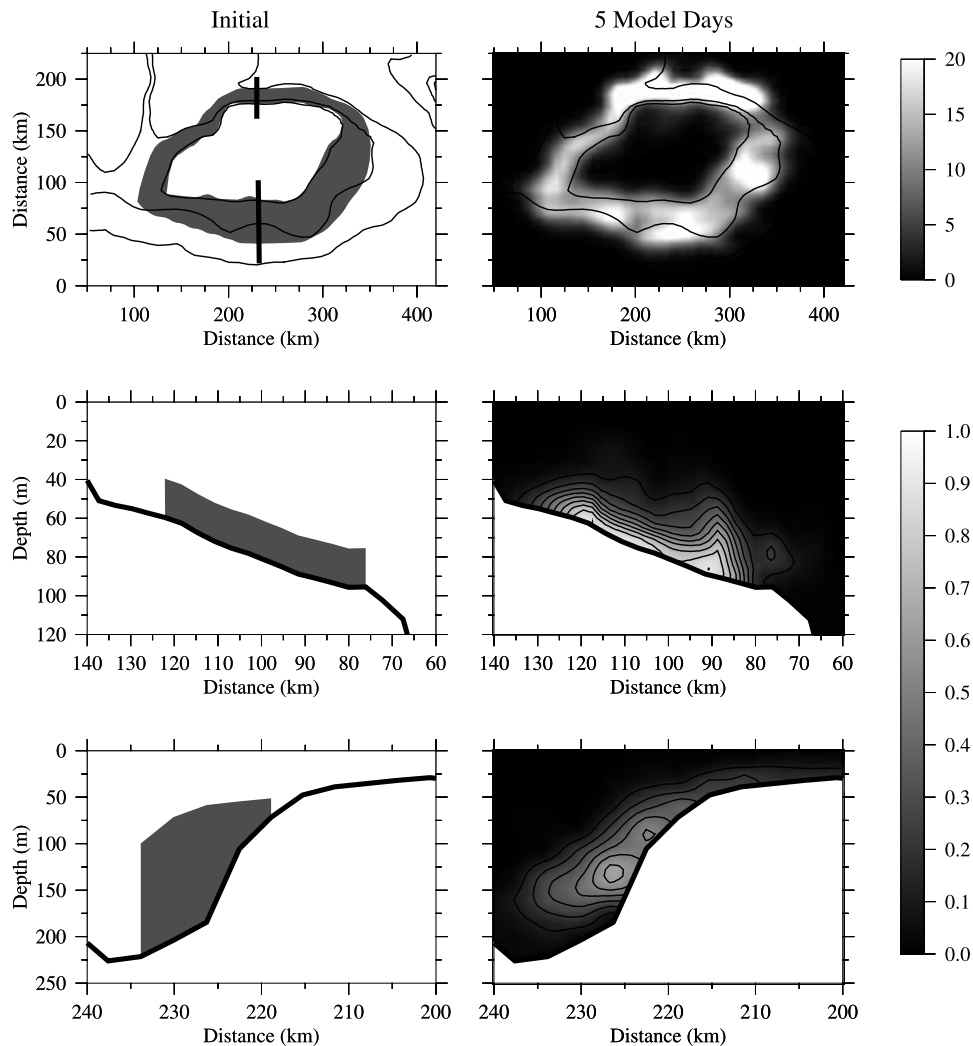


Figure 17. Distributions of a passive tracer at the initial time of release (left) and after 5 model days (right) for the case with tide only forcing (advection) and no diffusion. The tracer was released in the July–August stratified flow field at the 10th day and then traced for 30 days. Upper: the vertically integrated tracer concentration; middle: the cross-bank tracer distribution on the southern flank; and lower: the cross-bank tracer distribution on the northern flank. The locations of the northern and southern flank sections are shown as heavy lines in the upper left panel. The 60-, 80-, and 200-m depth contours are shown in the top panels.

velocity at 40 m) is reduced. Varying A_o has no significant impact on the direction of the particle trajectories since it is in general one order of magnitude smaller than U_s . The key parameter that controls the direction of the particle trajectories is the ratio of tidal excursion scale ($l_o = \frac{U_s}{\omega}$) to the topographic length scale L_s . l_o is about 8.5 km in our experiments, which is about two times smaller than $L_s = 20$ km in the first case and the same order with $L_s = 10$ km in the second case. The change in the particle movement found in the second case is clearly due to the strong nonlinearity of tidal currents over a steep bottom slope as suggested in the scale analysis by *Chen and Beardsley* [1998].

[50] It should be noted here that the specific particle drift direction in the case of periodic tidal flow depends on the phase of the tide at the time of the particle release. The drift results described above would be different if the release was made at a different time during the tidal period. The

discussion above only demonstrate only that the residual Lagrangian current can oppose the Eulerian current as the bottom slope becomes steep.

8. Discussion and Conclusions

[51] Characteristics of the cross-frontal water exchange on Georges Bank have been investigated through fluid particle tracking experiments conducted with a 3-D numerical circulation model with realistic topography, bi-monthly averaged initial stratification, and tidal and surface wind stress forcing. These model experiments suggest two primary paths for on-bank, cross-frontal water transport: one at the northwestern flank of GB where the bottom topography changes sharply in both along- and cross-bank directions, and the second near the bottom around the bank where the tidal mixing front is located. At the northwestern edge of the

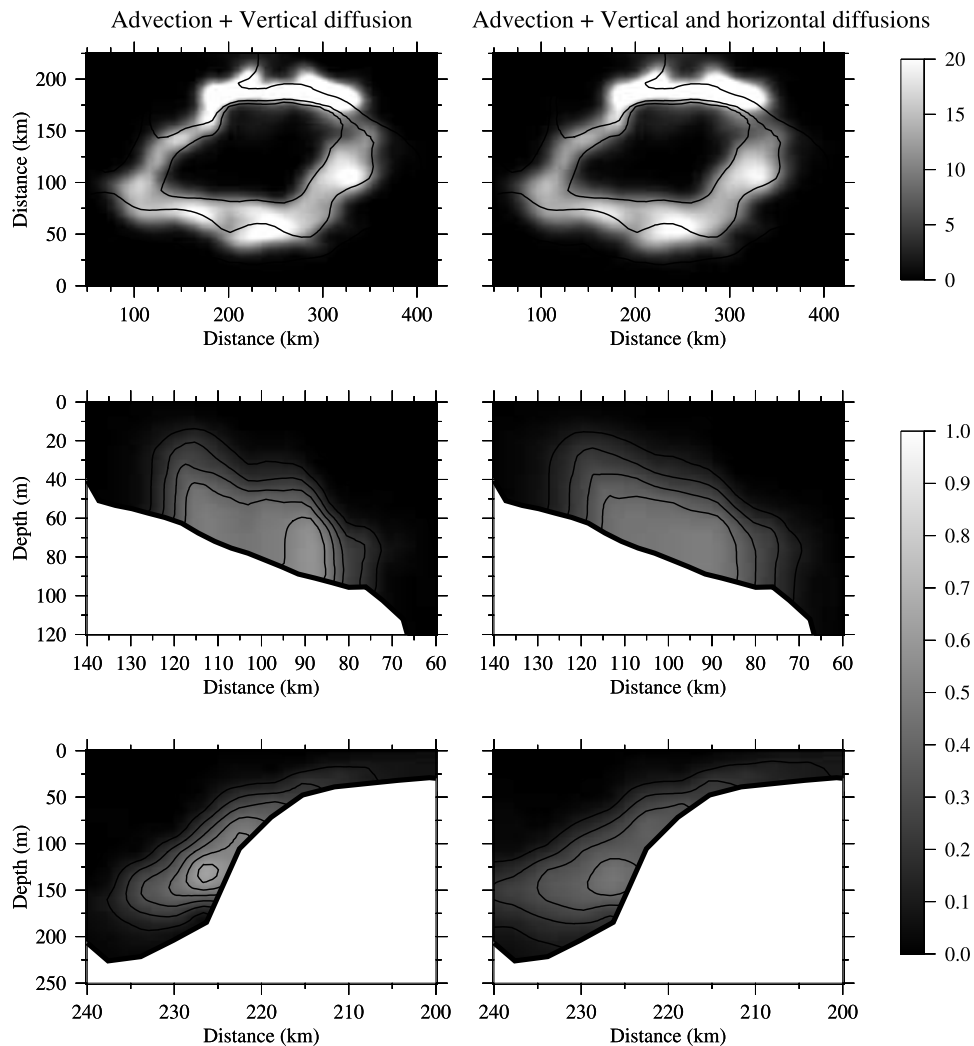


Figure 18. Distributions of the passive tracer after 5 model days for the cases with advection plus vertical diffusion (left) and advection plus vertical and horizontal diffusions (right). The tracer was released in the July–August stratified flow field at the 10th day and then traced for 30 days. (Upper) The vertically integrated tracer concentration. (Middle) The cross-bank tracer distribution on the southern flank. (Lower) The cross-bank tracer distribution on the northern flank.

GB, the strong cross-isobath flow occurs in all seasons, and accounts for the most significant on-bank water transport over GB. On the northern flank, the cross-bank component of the Lagrangian residual current is generally opposite in direction to that of the Eulerian residual current, resulting in a strong on-bank, cross-frontal flow along the bottom. On the southern flank in the zone between the tidal mixing and shelf-break fronts, the near-bottom particles move toward both fronts, causing a near-bottom divergence in this zone.

[52] The response of the model flow to wind-forcing varies with water depth. In winter, the strong wind stress tends to drive a significant off-bank water transport that can lead to a “washout” of the bank’s near-surface waters. The washout events, however, are generally restricted to the surface Ekman layer in the upper water column with little influence on the bottom flow except during extreme storms. In summer, the wind is too weak to alter the general pattern of tidal-driven particle trajectories within the mixed region and at the tidal mixing front. Some wind-driven off-bank

flow occurs near the surface in the stratified region on the outer southern flank, but there is little change in the near-bottom flow field. The wind-driven off-bank transport is larger in the case of time-dependent wind stress forcing than in the case with steady forcing, even though the total input of momentum is the same in both cases.

[53] To help check the results of the particle tracking experiments, experiments were conducted with summer stratification and tidal forcing in which a passive tracer was placed near the bottom over the bank and followed over many tidal periods. Evolution of the tracer field by advection only reveals a flux of tracer across the tidal mixing front into the mixed region on top of the bank. The addition of vertical diffusion allows an upward flux of tracer that reduces the near-bottom cross-front flux, while horizontal diffusion tends to increase the cross-front flux.

[54] As a further test of the model residual Lagrangian flow results, particles were tracked in an idealized 2-D flow field chosen to mimic the tidal and residual Eulerian flow

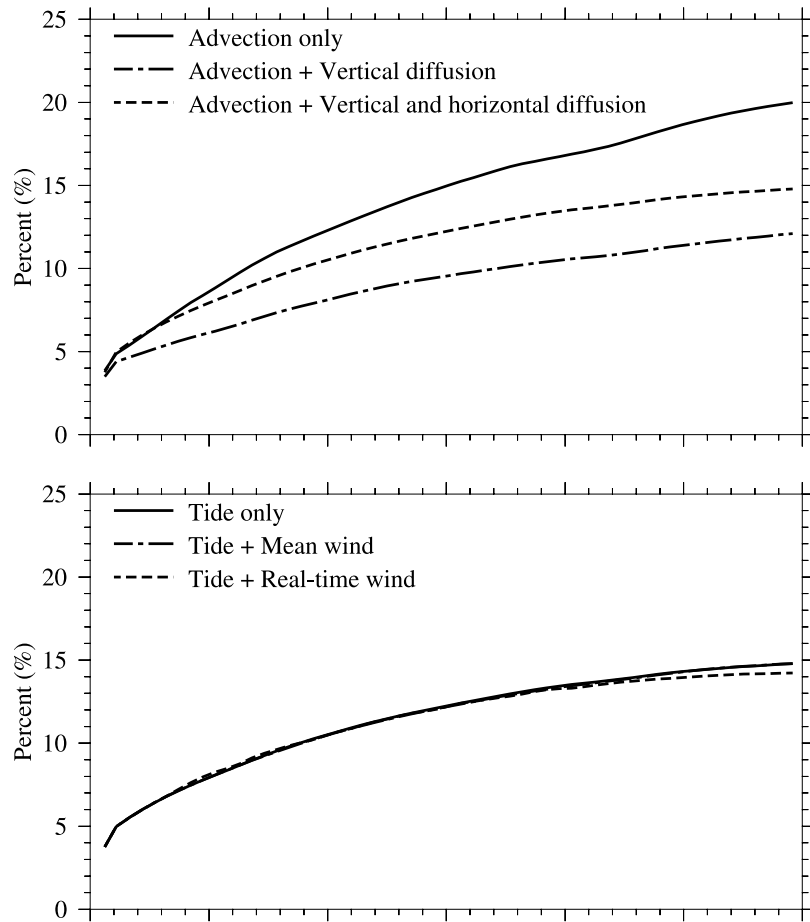


Figure 19. Percentage of tracer found within the crest control volume for the three cases with advection only (solid line), advection plus vertical diffusion (semidashed line), and advection plus vertical and horizontal diffusion (dashed line) for the case of tide only forcing (upper). Comparison of the cross-frontal tracer volumes for the cases of tide only forcing (solid line), tide and mean wind-forcing (semidashed line), and tide plus time-dependent wind-forcing (dashed line) with no diffusion (lower).

over the northern flank of the bank. For a given tidal and residual flow, the direction of the tidal-cycle residual particle trajectories is sensitive to the bottom slope. For small slope, the particle residual motion follows the Euler-

ian residual flow. For large slope, the particle motion can reverse and move opposite to the Eulerian residual flow. The direction of the particle trajectories depends on the nonlinearity of the tidal motion that can be estimated based

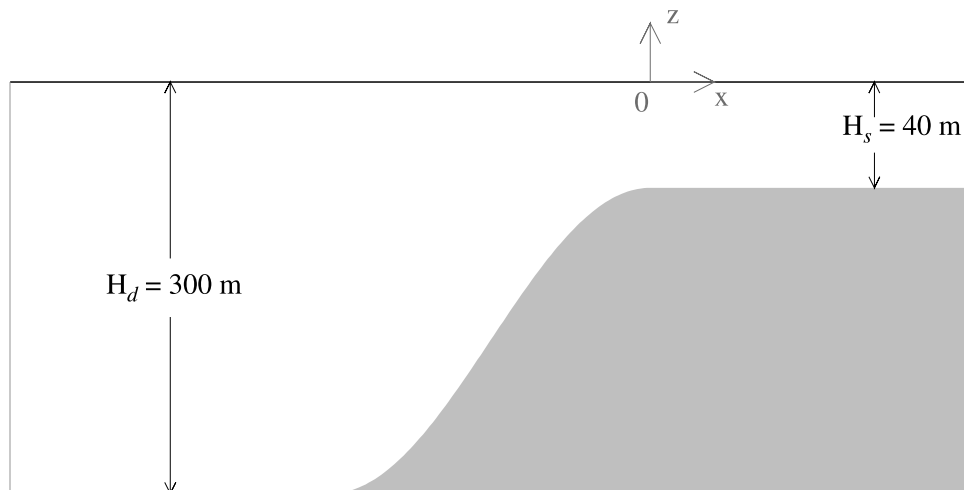


Figure 20. The 2-D model domain.

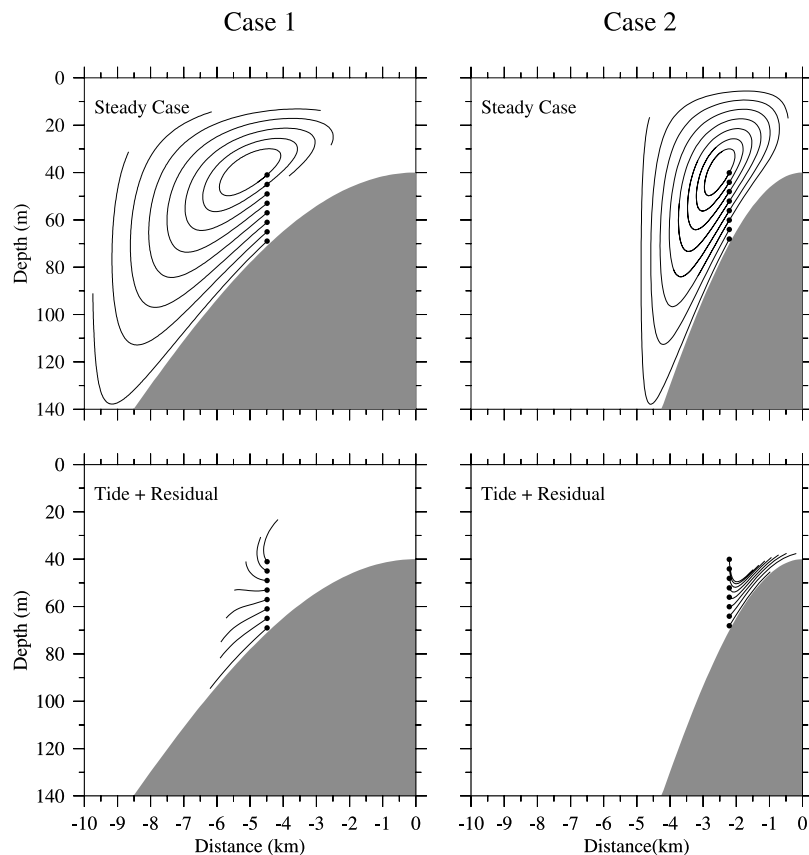


Figure 21. Residual particle trajectories for the cases without (steady state) and with tidal components. In the cases shown in the left panel, $L_S = 20$ km, $z_B = 1$ m, U_S (at $H = 40$ m) = 1.2 m/s. In the cases shown in the right panel, $L_S = 10$ km, $z_B = 1$ m, U_S (at $H = 40$ m) = 1.2 m/s. The maximum bottom slope is 0.013 for the case with $L_S = 20$ km and 0.026 in the case with $L_S = 10$ km.

on the ratio of the tidal excursion scale to the topographic length scale.

[55] The model results presented here are in general consistent with previous model experiments on GB conducted by *Loder et al.* [1997] and *Chen and Beardsley* [1998]. The near-surface particle trajectories predicted in our experiments are similar to observed Lagrangian drifter tracks described by *Limeburner and Beardsley* [1996] and *Naimie et al.* [2001]. The near-bottom convergence flow found at the shelf-break front on the southern flank supports the theoretical model predictions of *Chapman and Gawarkiewicz* [1993], *Gawarkiewicz* [1993], and *Chapman and Lentz* [1994].

[56] Recently, during the 1999 U.S. GLOBEC Northwest Atlantic/Georges Bank phase III studies, a fluorescent dye was injected into the stratified region of the bottom mixed layer on the southern and northern flanks of GB and tracked for several days to measure directly the near-bottom cross-bank Lagrangian flow [*Houghton and Ho*, 2001]. The dye mixed vertically throughout the bottom mixed layer and moved toward the tidal mixing front. A mean on-bank Lagrangian velocity of the dye was about 1.9 cm/s on the southern flank and 3.2 cm/s on the northern flank, which is in good agreement with the model-predicted mean Lagrangian velocity of about 1.5–2.2 cm/s on the southern flank and about 3.0 cm/s on the northern flank. This suggests that our model-predicted Lagrangian flow in this present study is

robust. Using diffusivities estimated from the dispersion of the dye patch, *Houghton and Ho* [2001] found that vertical mixing was primarily responsible for modifying the T/S properties of the water as it flowed across the tidal mixing front. Our tracer experiments show that the vertical diffusion within the frontal zone tended to reduce the cross-frontal water exchange on GB, which appears to be consistent with the dye tracking results. It should be pointed out that the reduction of cross-frontal water exchange due to vertical diffusion also applies to the near-bottom scalars. After tracers are diffused upward into the upper water column, the cross-frontal transport of these scalars would be controlled by the interaction of the tidal-induced clockwise residual gyre and wind-induced currents. In addition, the cross-bank horizontal diffusion coefficient derived by R. Houghton (personal communication) from the dye patch evolution was roughly the same (20 m²/s) as used in our model experiments. A more detailed model simulation of the 1999 dye experiment will be conducted as part of the U.S. GLOBEC phase IV analysis effort.

[57] Our results with realistic 3-D model topography support the 3-D spatial distribution of model-predicted nutrients and phytoplankton shown by *Franks and Chen* [1996, 2001]. Our fluid particle tracking experiments exhibit a strong residual near-bottom Lagrangian upwelling on the northern and northeastern flank, and a near-bottom convergent flow and hence upwelling at the tidal mixing

front on the southern flank. This pattern of vertical motion helps explain the high concentration of nutrients usually found around the tidal mixing front on GB during summer [Horne *et al.*, 1989]. The strong cross-isobath flow found on the northwestern flank may be a major on-bank pathway for copepods and perhaps larval fish in late spring and summer.

[58] The fact that fluid particles over the northern flank of GB generally move in the opposite direction to the Eulerian residual flow raises a critical issue in the methodology of estimating cross-frontal water and nutrient fluxes. This finding supports Loder and Horne's [1991] suggestion that the "skew flux," which arises when a strong nonlinear tidal flow exists in a scalar field with spatial gradients, must be taken into account when the nutrient flux onto GB is estimated.

[59] **Acknowledgments.** This research was supported by the U.S. GLOBEC Northwest Atlantic/Georges Bank program through NOAA grants NA56RG0487, NA960P003, and NA960P005 to Changsheng Chen, NSF grants OCE 96-32357 and OCE 98-06379 to Robert Beardsley, and NOAA grant NA76GP0176 to Peter Franks. Support for Qichun Xu was provided through Chen's NOAA grants. Two anonymous reviewers provided excellent comments and suggestions that improved this paper. This is U.S. GLOBEC contribution number 361.

References

- Beardsley, R. C., S. J. Lentz, R. A. Weller, R. Limeburner, J. D. Irish, and J. B. Edson, Surface forcing on the southern flank of Georges Bank, February–August 1995, submitted to *J. Geophys. Res.*, 2002.
- Blumberg, A. F., and G. L. Mellor, A description of a three-dimensional coastal ocean circulation model: Three-Dimensional Coastal Models, in *Coastal and Estuarine Sciences*, vol. 5, edited by N. Heaps, pp. 1–16, AGU, Washington, D. C., 1987.
- Casulli, V., Semi-implicit finite-difference methods for the two-dimensional shallow water equations, *J. Comput. Phys.*, 86, 56–74, 1990.
- Chapman, D. C., and G. Gawarkiewicz, One the establishment of the seasonal pycnocline in the Middle Atlantic Bight, *J. Phys. Oceanogr.*, 23, 2487–2492, 1993.
- Chapman, D. C., and S. J. Lentz, Trapping of a coastal density front by the bottom boundary layer, *J. Phys. Oceanogr.*, 24, 1464–1479, 1994.
- Chen, C., and R. C. Beardsley, Numerical study of stratified tidal rectification over finite-amplitude banks, Part I, Symmetric banks, *J. Phys. Oceanogr.*, 25, 2090–2110, 1995.
- Chen, C., and R. C. Beardsley, Tidal mixing and cross-frontal particle exchange over a finite amplitude asymmetric bank: A model study with application to Georges Bank, *J. Mar. Res.*, 56, 1165–1201, 1998.
- Chen, C., R. C. Beardsley, and R. Limeburner, Numerical study of stratified tidal rectification over finite-amplitude banks, Part II, Georges Bank, *J. Phys. Oceanogr.*, 25, 2111–2128, 1995.
- Chen, C., R. Beardsley, and P. J. S. Franks, A 3-D prognostic numerical model study of the Georges Bank ecosystem, Part I, Physical model, *Deep Sea Res. II*, 48, 419–456, 2001.
- Egbert, G. D., A. F. Bennett, and M. G. G. Foreman, TOPEX/POSEIDON tides estimated using a global inverse model, *J. Geophys. Res.*, 99, 24,821–24,852, 1994.
- Flagg, C. N., Hydrographic structure and variability, in *Georges Bank*, edited by R. H. Backus, pp. 108–124, The MIT Press, 1987.
- Franks, P. J. S., and C. Chen, Plankton production in tidal fronts: A model of Georges Bank in summer, *J. Mar. Res.*, 54, 631–651, 1996.
- Franks, P. J. S., and C. Chen, A 3-D prognostic numerical model study of the Georges Bank ecosystem, Part II, Biological-physical model, *Deep Sea Res. II*, 48, 457–482, 2001.
- Galperin, B., L. H. Kantha, S. Hassid, and A. Rosati, A quasi-equilibrium turbulent energy model for geophysical flows, *J. Atmos. Sci.*, 45, 55–62, 1988.
- Gawarkiewicz, G., Steady wind forcing of a density front over a circular bank, *J. Mar. Res.*, 51, 109–134, 1993.
- Horne, E. P. W., J. W. Loder, W. G. Harrison, R. Mohn, M. R. Lewis, B. Irwin, and T. Platt, Nitrate supply and demand at the Georges Bank tidal front, *Sci. Mar.*, 53, 145–158, 1989.
- Houghton, R. W., and C. Ho, Diapycnal flow through the Georges Bank tidal front: A dye tracer study, *Geophys. Res. Lett.*, 28, 33–36, 2001.
- Limeburner, R., and R. C. Beardsley, Near-surface recirculation over Georges Bank, *Deep-Sea Res. II*, 43, 1547–1574, 1996.
- Loder, J. W., and E. P. W. Horne, Skew eddy fluxes as signatures of nonlinear tidal current interactions, with application to Georges Bank, *Atmos.-Ocean*, 29(3), 517–546, 1991.
- Loder, J. W., and D. G. Wright, Tidal rectification and front circulation on the sides of Georges Bank, *J. Mar. Res.*, 43, 581–604, 1985.
- Loder, J. W., Y. Shen, and H. Ridderinkhof, Characterization of three-dimensional Lagrangian circulation associated with tidal rectification over a submarine bank, *J. Phys. Oceanogr.*, 27, 1729–1742, 1997.
- Maas, L. R. M., and J. T. F. Zimmerman, Tide-topography interaction in a stratified shelf sea, I, Basic equations for quasi-nonlinear internal tides, *Geophys. Astrophys. Fluid Dyn.*, 45, 1–35, 1989a.
- Maas, L. R. M., and J. T. F. Zimmerman, Tide-topography interaction in a stratified shelf sea, II, Bottom trapped internal tides and baroclinic residual currents, *Geophys. Astrophys. Fluid Dyn.*, 45, 37–69, 1989b.
- Mellor, G. L., and T. Yamada, A hierarchy of turbulence closure models for planetary boundary layers, *J. Atmos. Sci.*, 33, 1791–1896, 1974.
- Mellor, G. L., and T. Yamada, Development of a turbulence closure model for geophysical fluid problem, *Rev. Geophys. Space Phys.*, 20, 851–875, 1982.
- Naimie, C. E., J. W. Loder, and D. R. Lynch, Seasonal variation of the 3-D residual circulation on Georges Bank, *J. Geophys. Res.*, 99, 15,967–15,989, 1994.
- Naimie, C. E., Georges Bank residual circulation during weak and strong stratification periods: Prognostic numerical model results, *J. Geophys. Res.*, 101(C3), 6469–6486, 1996.
- Naimie, C. E., R. Limeburner, C. G. Hannah, and R. C. Beardsley, Comparison between numerically simulated and observed drifter trajectories on Georges Bank, *Deep Sea Res. II*, 48, 501–518, 2001.
- Pringle, J. M., and P. J. S. Franks, Asymmetric mixing transport: A horizontal transport mechanism for sinking plankton and sediment in tidal flows, *Limnol. Oceanogr.*, 46(2), 381–391, 2001.
- Roworth, E., and R. Signell, Construction of digital bathymetry for the Gulf of Maine, (<http://orale.er.usgs.gov/GoMaine/bathy/index.htm>), 1998.
- Smolarkiewicz, P. K., A fully multidimensional positive definite advection transport algorithm with small implicit diffusion, *J. Comput. Phys.*, 54, 325–462, 1984.
- Smolarkiewicz, P. K., and T. L. Clark, The multidimensional positive definite advection transport algorithm: Further development and applications, *J. Comput. Phys.*, 67, 396–438, 1986.
- Smolarkiewicz, P. K., and W. W. Grabowski, The multidimensional positive definite advection transport algorithm: Nonoscillatory opinion, *J. Comput. Phys.*, 86, 355–375, 1990.

R. C. Beardsley, Department of Physical Oceanography, Woods Hole Oceanographic Institution, Woods Hole, MA 02543, USA. (rbeardsley@whoi.edu)

C. Chen and Q. Xu, School for Marine Science and Technology, University of Massachusetts-Dartmouth, New Bedford, MA 02747-1221, USA. (clchen@umassd.edu; qxu@umassd.edu)

P. J. S. Franks, Marine Life Research Group, Scripps Institution of Oceanography, University of California, San Diego, La Jolla, CA 92093-0218, USA. (pfranks@ucsd.edu)